Establishment and Optimization of Super-Resolution Fluorescence Microscopy for Multi-Colour Studies of Biological Systems

Masterarbeit aus dem Fachgebiet

Physikalische Chemie

von

B.Sc. Jens Prescher

geboren am 17.12.1984
in München

für die Masterprüfung in Chemie an der
Ludwig-Maximilians-Universität München

Datum der mündlichen Prüfung: 04.02.2010
Beginn der Masterarbeit: 15.02.2010

Masterarbeit beim Prüfungsausschuss eingereicht am 16.08.2010

Erklärung

Ich versichere, dass ich die vorliegende Masterarbeit am Department Chemie (Lehrbereich Physikalische Chemie) der Ludwig-Maximilians-Universität München unter der Anregung und Anleitung von Prof. Don C. Lamb, PhD selbstständig durchgeführt und keine anderen als die angegebenen Hilfsmittel und Quellen benutzt habe.

München, den 16.08.2010 ______________________________

Erstgutachter: Prof. Don C. Lamb, PhD

____

Zweitgutachter: Prof. Dr. Christoph Bräuchle

„Nature is colorful. Even before men lived upon the earth the sky was blue, the forests green, the rocks gray, the soil brown. Sunrises and sunsets splashed golds and reds across the horizon, and from every summer shower the rainbows arched.“

Hanor A. Webb, *Journal of Chemical Education*, 19, **1942**.

Danksagung

An erster Stelle möchte ich Prof. Don Lamb für die großartige Möglichkeit danken, diese Masterarbeit in seiner Gruppe anfertigen zu können, für all die Unterstützung und Ratschläge und für die hervorragende Arbeitsatmosphäre!

An dieser Stelle auch vielen Dank an Prof. Christoph Bräuchle für die stetige Unterstützung bei der Umsetzung des HIV-Projekts sowie für die Übernahme des Zweitgutachtens!

Mein besonderer Dank gilt außerdem Sergey für die fantastische Betreuung während der letzten sechs Monate. Vielen Dank für all die Unterstützung und Hilfe, für das Erklären physikalischer und mathematischer Zusammenhänge (ganz egal, welche Frage man hat, es ist sehr selten, dass Sergey sie nicht beantworten kann!) und fürs Probelesen!

Monika danke ich für die Vorbereitung all der Zellkulturen, ohne die so gut wie keiner der Versuche in dieser Arbeit durchzuführen gewesen wäre.

Vielen Dank auch an Vova für all die Programmierarbeit, die er für das STORM-Projekt geleistet hat!

Danke auch an alle übrigen Mitarbeiter der AKs Lamb, Bräuchle, Michaelis für die großartige Arbeitsatmosphäre und die Tatsache, dass egal, was für ein Problem man hat, immer jemand da ist, der einem weiterhelfen kann!

Contents

1 Introduction......7

1.1 Motivation......7

1.2 Aims of the thesis......11

2 Super-Resolution Fluorescence Microscopy......12

2.1 Basic principles of fluorescence......12

2.2 Widefield Fluorescence Microscopy......14

2.3 Total Internal Reflection Fluorescence Microscopy......15

2.4 Super-resolution Fluorescence Microscopy by STORM and PALM......20

2.4.1 General principle......20

2.4.2 Stochastic Optical Reconstruction Microscopy (STORM)......21

2.4.3 Photoactivated Localization Microscopy (PALM)......24

3 STORM and PALM imaging - measurement methods and analysis......27

3.1 Setup......27

3.1.1 Configuration......27

3.1.2 Calibration and mapping of EMCCD cameras......29

3.1.2.1 Image acquisition by EMCCD cameras......29

3.1.2.2 Camera calibration......31

3.1.2.3 Camera mapping......32

3.2 Optimization of measurement protocol......34

3.2.1 Used test systems......34

3.2.2 Optimization of data acquisition protocol......35

3.2.3 Optimization of measurement conditions for STORM......35

3.3 Image reconstruction......39

3.3.1 2D Gaussian Fitting......39

3.3.2 Non-fitting localization based on FluoroBancroft algorithm......42

3.3.2.1 Principle of the FluoroBancroft algorithm......43

3.3.2.2 Realization......45

3.3.3 Comparison of both localization methods......46

3.3.3.1 Calculation speed......46

3.3.3.2 Data quality......47

3.3.4 Drift correction using cross correlation......53

3.4 Discussion and outlook......55

4 Study of HIV budding by Super-Resolution Fluorescence Microscopy......58

4.1 Project overview and background......58

4.2 Experimental approach......60

4.3 Results......62

4.4 Discussion and outlook......66

5 Methods........68

5.1 Materials........68

5.2 Buffers........70

5.3 Sample preparation........71

5.3.1 Preparation and fixation of streptavidin-labelled beads........71

5.3.2 Preparation and fixation of cell samples........72

6 Attachments........75

6.1 Abbreviations........75

6.2 References........76

1 Introduction

1.1 Motivation

Throughout history, humanity has always been striving to study and understand the marvellous wonders of nature. However, the natural resolution limit of the unaided human eye did not allow the study of objects smaller than 0.1 mm, therefore hindering scientists from entering the world of microorganisms. Because of this lack of knowledge, many natural processes like infections or diseases were not explained satisfactorily. It was only with the invention of the first microscopes that a deeper understanding could be obtained.

Although the magnifying effect of simple lenses was already known in Ancient Rome, it was not until the end of the 16th century when Hans and Zacharias Janssen made first steps in the development of the first optical microscope. However, the importance of this tool was not fully recognised until the middle of the 17th century when two scientists demonstrated the relevance of this tool. Fig. 1.1 shows a scheme of an improved version of a compound microscope (a microscope using more than one lens) that was presented by Englishman Robert Hooke in 1665:

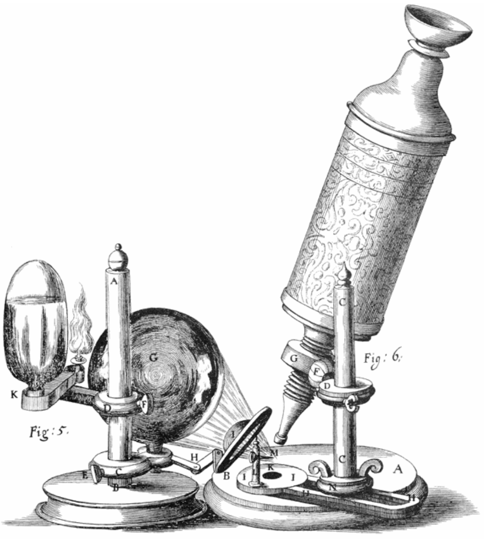

Figure 1.1: Drawing of Hooke's microscope, taken from [1]

With this tool, Hooke was able to observe the structure of small objects like insects or parts of plants. Also his studies of plant anatomy made him establish the term *cell* for the well-defined-structures he observed.

Inspired by Hooke's work, Dutch scientist Antoni van Leeuwenhoek was able to improve the manufacture of glass lenses. These new lenses enabled him to resolve even smaller objects although he used only one-lens systems as depicted in fig. 1.2 instead of compound microscopes as Hooke did:

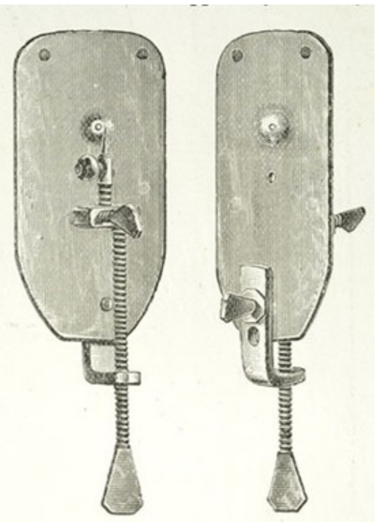

FIGURE 1.2: MODEL OF LEEUWENHOEK'S MICROSCOPE, TAKEN FROM [2]

In 1675, Leeuwenhoek was able to observe, for the first time, microorganisms like bacteria in rainwater which he originally called 'animalcules' [3]. This was the beginning of a completely new understanding of natural processes. For example, it was van Leeuwenhoek who could falsify the ruling opinion that small animals like fleas and mussels spontaneously develop from dirt and earth, but could show that they lay eggs.

The huge impact these discoveries had for scientific community as well as for the public is apparent. For example, the causative organisms for diseases could now be identified and for this reason they could also be fought. It was no longer necessary to take them as god-given plagues.

The next big step in the history of optical microscopy was the construction of the first fluorescence microscope in 1911 by Oskar Heimstädt [4]. Due to several reasons, the field of application for this new technique was limited at first: For example, one could only rely on autofluorescence of the cell at the beginning until this problem was solved by Max Haitinger who, among other scientists, showed that it is possible to label biological samples with externally applied dyes and in 1941, Albert Coons was the first to use fluorescent labelled antibodies to stain particular organelles of the cell [5].

Another problem was regarding the excitation light as light sources at that time did not provide enough power to excite fluorophores at a high enough rate. This was overcome by the development of the first lasers in the 1960s, which offered a bundled, high energetic, monochromatic and coherent beam that was effectively able to excite fluorescent samples.

Also, an effective separation of the fluorescence signal from the excitation light was required. Heimstädt had to use darkfield illumination, a method that is technically complex. Hence, the invention of the epifluorescence microscope in 1929 by Philipp Ellinger and August Hirt was a great step forward [6] which was finally completed by the development of dichroic mirrors in 1967 [7]. Dichroic mirrors offered an elegant way to separate the fluorescence signal from the excitation light by only reflecting well defined regions of the electromagnetic spectrum and letting the others pass (cf. chapter 2). This last aspect was especially responsible for the wide spread and powerful application possibilities of fluorescence microscopy for the biophysical sciences.

Due to the progress in the study of inter-cellular processes and interactions, soon the resolution limit of optical microscopes was reached. Diffraction of the light on the microscope aperture limits the resolution of optical microscopy to around 200 nm (cf. chapter 2). For this reason, scientists were striving to develop new methods which would surpass this limit. At the end of the 20th century, several possibilities were discovered on how the resolution power of an optical microscope can be extended by a factor of 10 down to a limit of about 10-20 nm by using techniques like Stimulated Emission Depletion (STED), Stochastic Optical Reconstruction Microscopy (STORM) or Photoactivated Localization Microscopy (PALM) [8]. The latter two will be discussed in detail in this thesis.

On the contrary, a great number of other, non-optical techniques were presented that offer an even higher resolution than these high-resolution optical microscopes. Examples for this include Scanning Electron Microscopy (SEM) with a resolution up to 3 nm, X-ray tomography (5 nm) or Transmission Electron Microscopy (TEM) (0.1 nm). However, optical microscopy holds significant advantages compared to these other methods, so that this slight loss on resolution is acceptable. Not only can it be realised with a relatively low technical effort and at low costs compared to e.g. SEM and TEM, but it is also appropriate for studying biological samples. Optical microscopy experiments can be performed at room temperature and normal pressure and no complex sample preparation is necessary. For example, metal coating is required for SEM in order to make biological samples conductive for the electrons.

Optical microscopy as a non-invasive method even allows for the studying of living organisms and thereby the imaging of dynamic processes. Furthermore, it is a method that cannot only be applied to surfaces (like SEM) or very thin structures (like TEM), but makes it possible to study the entire volume of a cell.

Another advantage compared to non-optical microscopy techniques (e.g. scanning electron microscopy) is the possibility to obtain multi-coloured pictures by labelling different parts of the sample with differently coloured dyes which can facilitate the distinction of these structures in the sample as is demonstrated in fig. 1.3. In this two-colour-STORM experiment [9], the microtubuli and clathrin coated pits (CCPs) of a mammalian cell were stained by differently labelled antibodies. This example impressively proves the relevance of these high-resolution fluorescence microscopy methods.

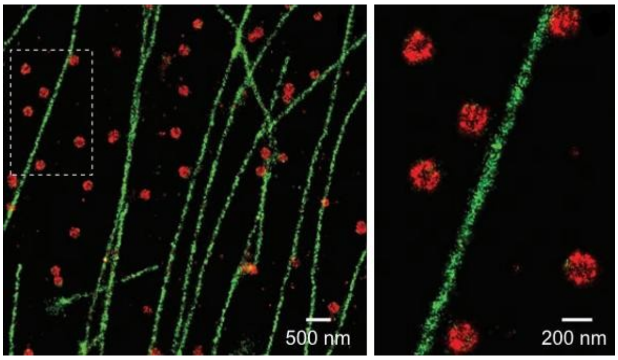

FIGURE 1.3: EXAMPLE OF A TWO-COLOUR-STORM EXPERIMENT: MICROTUBULI (GREEN) AND CLATHRIN COATED PITS (RED) OF A MAMMAL CELL, TAKEN FROM [9]

1.2 Aims of the thesis

Localization microscopy methods for Super-Resolution Fluorescence Microscopy like PALM and STORM offer an elegant possibility to surpass the resolution limit of classic optical microscopy and therefore allow the investigation of structures whose details would have otherwise remained hidden. For this reason, both methods will be established and optimized during the course of this study.

In chapter 2, the theoretical background of fluorescence microscopy and the applied super-resolution methods will be presented before the next chapter will address the experimental approach. Here, the optimization of the measurement conditions will be discussed in sections 3.1 and 3.2 and two different methods for data evaluation will be presented in section 3.3. Appropriate tools for error correction will be implemented into the data evaluation routine in order to optimize the quality of these methods, which will be subsequently tested on simulated data regarding evaluation speed and accuracy. Furthermore, they will be applied to model systems like polystyrene beads and cellular microtubuli.

Following, PALM and STORM will be used for studying the budding process of HI-viruses in chapter 4. It was shown that HIV has to recruit cellular ESCRT complex during this process [10]; however, many questions concerning the interaction of HIV proteins with the ESCRT proteins are still open. Here, PALM and STORM appear as ideal methods to study these interactions due to their multi-colour approach therefore demonstrating the potential of Super-Resolution Fluorescence Microscopy.

2 Super-Resolution Fluorescence Microscopy

2.1 Basic principles of fluorescence

Fluorescence is a form of photoluminescence. This more general term describes an optical process in which the molecular absorption of a photon leads to the excitation of an electron to a higher energetic state followed by relaxation to the ground state accompanied by the emission of another photon with a longer wavelength. The processes involved in fluorescence can be visualized by a Jablonski diagram as shown in fig. 2.1:

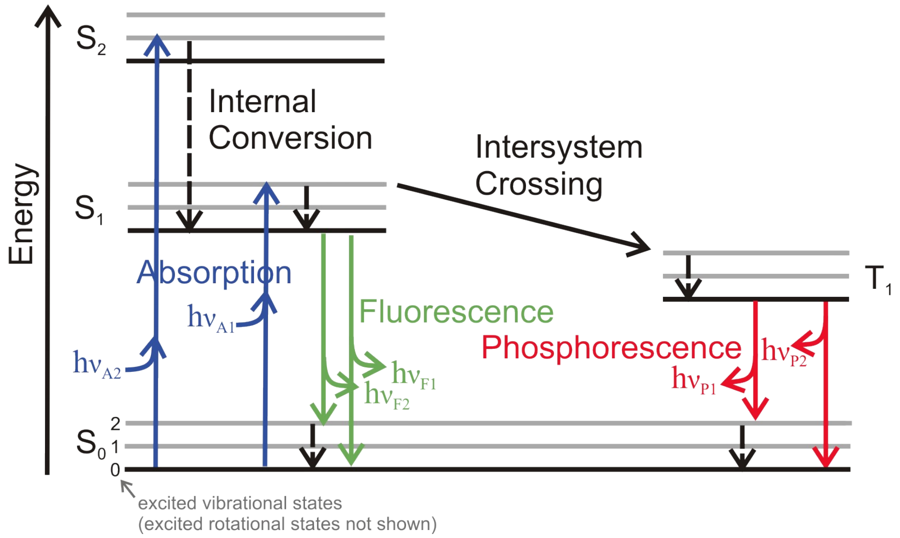
Energy
S_2
Internal Conversion
Intersystem Crossing
S_1
T_1
Absorption
$h\nu_{A1}$
$h\nu_{A2}$
Fluorescence
$h\nu_{F1}$
$h\nu_{F2}$
Phosphorescence
$h\nu_{P2}$
$h\nu_{P1}$
2
1
0
S_0
excited vibrational states
(excited rotational states not shown)

Figure 2.1: Example of a Jablonski diagram (S_n = n^{th} Singlet state, T_n = n^{th} Triplet state, ν_A = absorption frequency, ν_F = fluorescence frequency, ν_P = phosphorescence frequency), adapted from [11]

At the beginning, all molecules can be considered to be in the vibrational ground state of the lowest energetic singlet state S_0. When light is absorbed, an electron can be excited to an energetically higher singlet state (S_1 or higher). Usually, the electron does not end up in the vibrational ground state of this excited state but in a higher vibrational level. The probability, in which vibrational level the electron will end up, is determined by the Franck-Condon-Principle which is based on the Born-Oppenheimer approximation which states that nuclei displacement is slow compared to electron excitation (~ fs). This means that the nuclear position of the vibrational level of the new state must be compatible with the respective one in the originating state, a fact that is visualized by perpendicular transitions in the Jablonski diagram. Furthermore, this new vibrational level must be instantaneously compatible with the momenta of the vibrational level of the molecule in the originating electronic state, as the visualization of the

Franck-Condon-Principle in fig. 2.2a shows:

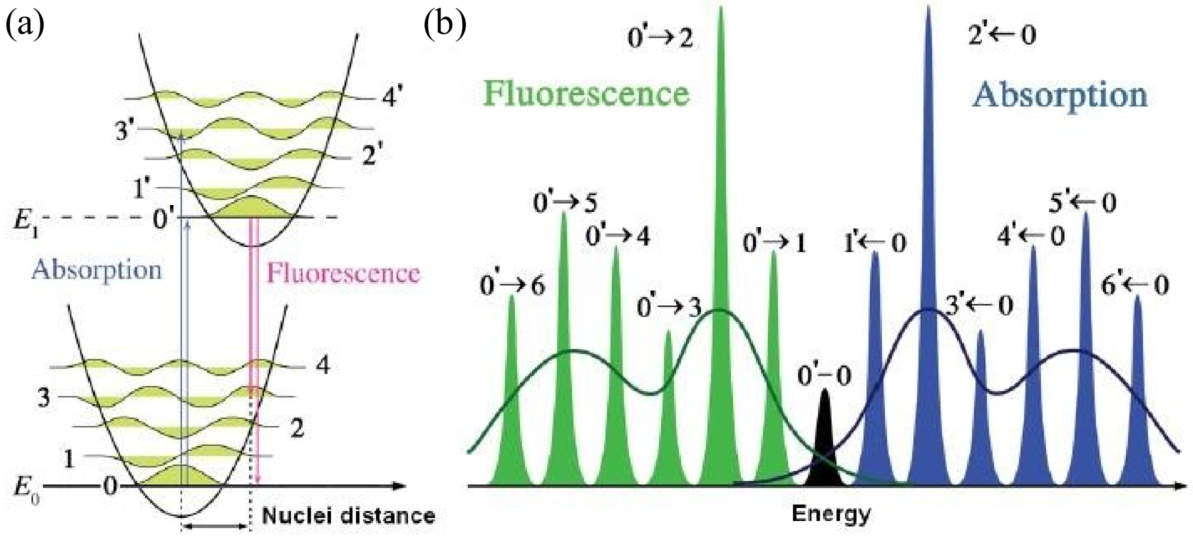

Figure 2.2: Visualization of the Franck-Condon-Principle (a) and the Stokes Shift (b), taken from [12]

The better the overlap of the wave functions of the different energetic states, the more likely is the corresponding transition which results in the different intensities in the absorption spectra shown in fig. 2.2b. Following excitation, the molecule will almost immediately relax radiationless to the vibrational ground state of S_1 by transfer of energy to the environment. This process is called Internal Conversion (IC) and occurs on a time scale in the range of picoseconds. From this metastable state with a lifetime in the order of nanoseconds, the molecule will relax to the energetic ground state either radiationless (IC) or by emitting the excess of energy in form of a photon. This process conforms to the rules given by the Franck-Condon-Principle analogous to absorption (cf. fig. 2.2). In consequence, the last step has to be another IC relaxation from an excited vibrational state of the energetic ground state to the corresponding vibrational ground state. Due to the loss of energy in the non-radiant processes the emission spectrum is shifted to a lower energetic range compared to the absorption spectrum (Stokes-Shift). The observed mirror symmetry of both spectra is a result of the assumption that the vibrational levels are equidistant in every S_N-state.

With a certain probability, however, it is also possible that the excited molecule undergoes an Intersystem Crossing from the singlet S_1 state to the triplet T_1 state. This transition is actually forbidden due to momentum conservation that defines the selection rules $\Delta l = \pm 1$ for orbit angular momentum and $\Delta s = 0$ for spin angular momentum. However, when the molecular weight increases, spin-orbit coupling becomes stronger which means that orbit and spin functions are not completely separable any longer. By this means, Intersystem Crossing is possible. However it is kinetically unfavoured. Hence, the molecule will be trapped in the vibrational ground state of T_1 after IC resulting in comparatively long times for relaxation to S_1 (ms – s). As opposed to fluorescence, this process is then called phosphorescence.

2.2 Widefield Fluorescence Microscopy

It was shown that fluorescence microscopy offers great benefits for the study of biological samples. The basic principle is quite simple: an object labelled with a fluorescent dye is irradiated with laser light of a wavelength matching with the absorption spectrum of the fluorophore. Because of the Stokes-Shift, the emitted fluorescence signal is characterized by a higher wavelength than the exciting beam. Hence, by using tools like dichroic beam splitters which reflect only well defined regions of the electromagnetic spectrum and let the others pass, excitation and detection pathway can be separated easily as shown in fig. 2.3:

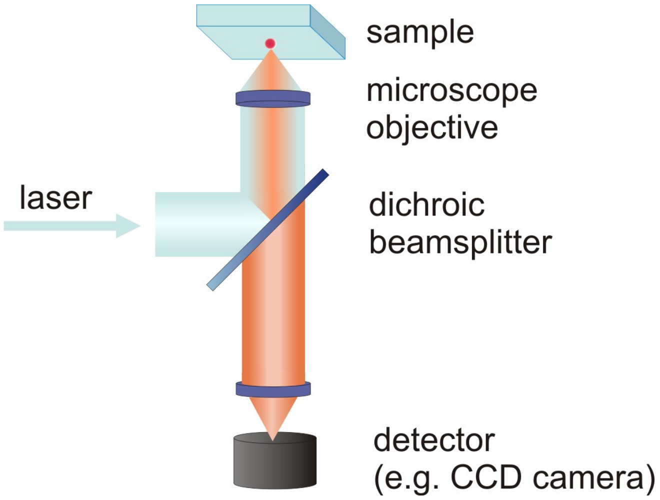

FIGURE 2.3: BASIC SCHEME OF A FLUORESCENCE MICROSCOPE (BLUE: EXCITATION PATHWAY, RED: DETECTION PATHWAY)

One fundamental limitation of classic fluorescence microscopy, however, lies in the confinement of the resolution power of a light microscope due to light diffraction on the aperture of the microscope objective. The resolution power can be described with the help of the so called point spread function (PSF) which expresses the intensity distribution of an ideal point-shaped object in the three-dimensional image space. The occurring diffraction – and for this reason also the PSF of conventional light microscopes – is determined by the wavelength of the light source λ as well as by the numeric aperture of the microscope *NA*. With these two values, the lateral resolution Δx can be estimated by equation 2.1:

$$\Delta x = 0.61 \frac{\lambda}{NA} \tag{2.1}$$

The numeric aperture NA is given by half of the angle of the aperture of the objective 2α and the refraction index n of the medium between objective and sample:

$$NA = n * \sin \alpha \tag{2.2}$$

The condition defined by these equations is called the Rayleigh criterion which is visualized in fig. 2.4:

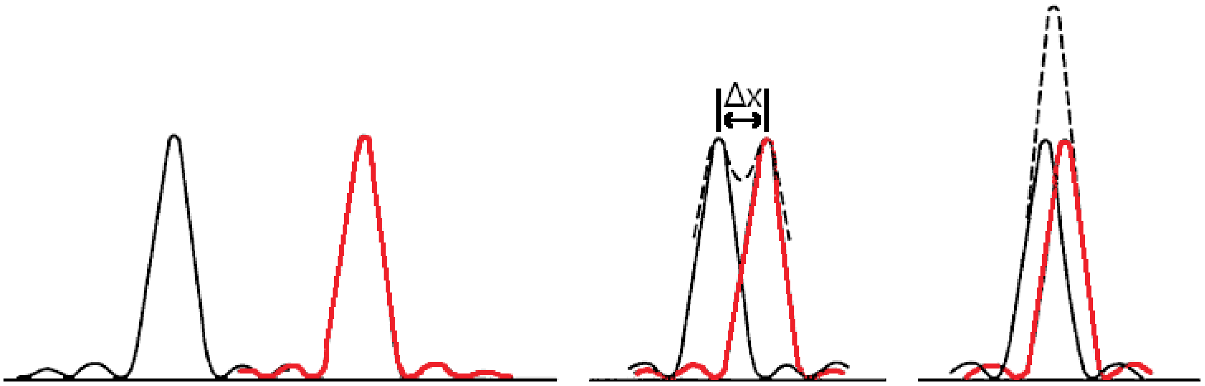

(a) resolvable **(b) Rayleigh criterion** **(c) not resolvable**

Figure 2.4: Visualization of the Rayleigh criterion: only signals with a greater distance than Δx are resolvable (dashed line in b) and c): merged image of both signals)

However, under certain circumstances, it is still possible to resolve two signals with a distance smaller than Δx. This is the case when the dip between the two peaks of the merged PSF as shown in fig 2.4b is deep enough to be visible at the given photon count rates. For this reason, the astrophysicist C. M. Sparrow presented another specification of the resolution limit (Sparrow-criterion) [13], which he defined as the distance from which on the dip cannot be observed any longer. For most applications, however, the Rayleigh-criterion is sufficient to describe the resolution capacity of the used system.

2.3 Total Internal Reflection Fluorescence Microscopy

Besides diffraction limiting the resolution, another problem arising in classical fluorescence microscopy is low contrast of the images due to high background noise. Especially when cells or other biological samples are investigated, which are – as described above – one main target of fluorescence microscopy, effects like biological autofluorescence may actually exceed sample fluorescence which results in poor image quality.

Besides of other methods like e.g. avoiding out-of-focus excitation and detection by confocal microscopy [14], Total Internal Fluorescence Reflection Fluorescence Microscopy (TIRFM) offers an elegant method for surface-sensitive microscopy that comes along with a relatively low technical effort. The basic idea of TIRFM is the usage of evanescent waves for excitation which are characterized by a very short range (~ 100 nm). Hence, only objects close to the surface of the sample can be excited. As the name TIRFM already suggests, these evanescent waves can be generated when the incoming laser light is totally reflected on the phase interface between the glass microscope slide and the aqueous medium of the sample. A basic scheme of this principle is shown in fig. 2.5, a detailed discussion of the method will follow below.

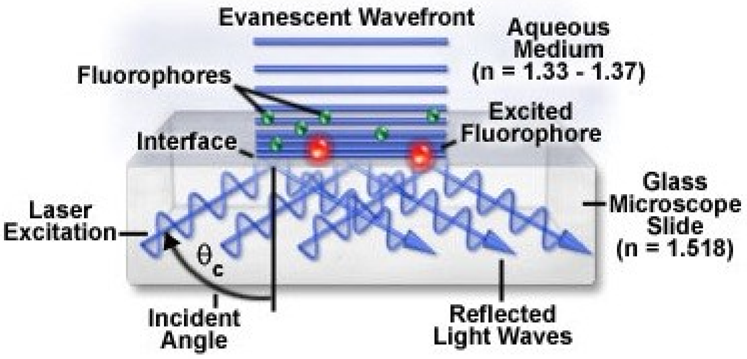

Figure 2.5: Basic scheme of TIRFM: incoming light that is totally reflected on the phase interface generates an evanescent wavefront that excites fluorophores of the sample, taken from [15]

To understand TIRFM in detail, some information about evanescent waves is required: In general, an electromagnetic wave in vector space that is constant in (x, y) and propagating in z can be described as:

$$\bar{E}(k_x, k_y, z) = \bar{E}(k_x, k_y, 0) * e^{\pm i k_z z} = \bar{E}(k_x, k_y, 0) * e^{\pm i z \sqrt{k^2 - k_x^2 - k_y^2}} \tag{2.3}$$

where the wave vector k of a wave with the wavelength λ is defined by $k = 2\pi/\lambda$ and $k^2 = k_x^2 + k_y^2 + k_z^2$. Now, one has to distinguish between two cases:

a) $k_x^2 + k_y^2 \leq k^2$

In this case k_z is a real number, therefore the imaginary unit in the exponential function is retained. Hence, using Euler's Formula, the wave propagating in $+z$ can be described as a sine or cosine wave.

b) $k_x^2 + k_y^2 \geq k^2$

Here k_z is imaginary, therefore the propagation in $+z$ is determined by the term $e^{-|k_z| z}$, which means that these waves, which are called evanescent waves, undergo an exponential decay with a decay length of $|1/k_z|$ which is typically in the range of around 100 nm.

In order to use evanescent waves as a source of excitation for surface sensitive TIRFM, it is necessary to generate an evanescent field that is separated from the propagating field. As it will be shown below, this is possible by using total internal reflection of the exciting light on the phase interface between sample and object slide. This effect and the conditions for its occurrence will be affiliated on the basis of fig. 2.6:

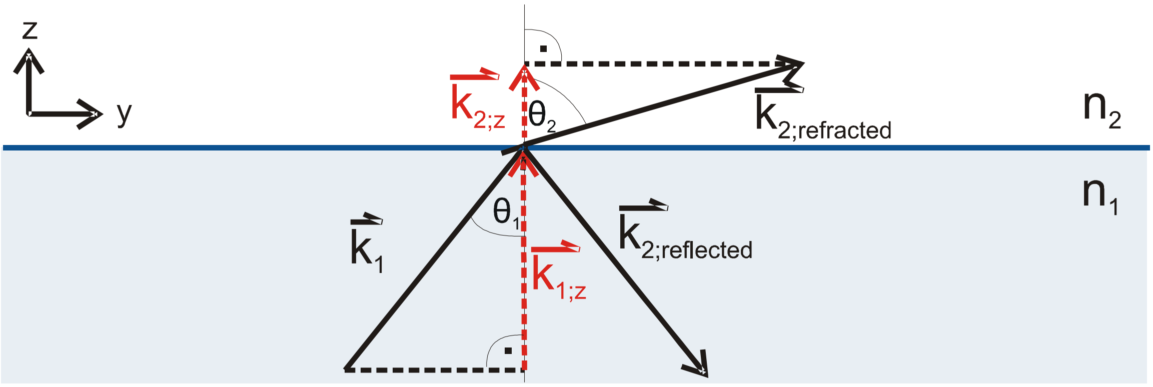

FIGURE 2.6: REFRACTION AND TOTAL INTERNAL REFLECTION ON A PHASE INTERFACE BETWEEN TWO MEDIA WITH REFRACTION INDICES n_1 AND n_2 (k_1 = INCOMING WAVE, k_2 = REFLECTED/REFRACTED WAVE WITH Z-COMPONENTS $k_{1;z}$ AND $k_{2;z}$)

In general, refraction on a phase interface can be described by Snell's law:

$$n_1 \sin\theta_1 = n_2 \sin\theta_2 \quad \text{or} \quad \sin\theta_2 = \frac{n_1}{n_2}\sin\theta_1 \tag{2.4}$$

If n_2 is smaller than n_1, the angle of refraction of the refracted beam θ_2 will be larger than the respective angle of the incoming beam θ_1 or in other words the beam will be further away from the perpendicular after passing the phase boundary. If θ_1 is now increased until θ_2 reaches the value of 90° (this value for θ_1 is called the critical angle θ_c), there will be no longer a refracted beam but the whole light is reflected on the surface in the direction of $k_{2;reflected}$ as shown in figure 2.6. This process is called total internal reflection and occurs for all angles θ_1 larger than θ_c. This can be described mathematically by setting $\theta_2 = 90°$ in equation 2.4. The whole term can then be rearranged to the following expression for the critical angle:

$$\sin\theta_c = \frac{n_2}{n_1} \tag{2.5}$$

Now, in order to understand why there is still an evanescent wave in the n_2 medium when the rest of the wave is reflected, it is necessary to look at the part of the refracted wave propagating in z-direction $k_{2;z}$ which is given by:

$$\cos\theta_2 = \frac{k_{2;z}}{k_{2;refracted}} \quad \text{or } k_{2;z} = k_{2;refracted}\cos\theta_2 \tag{2.6}$$

Replacing the cosine by a sine expression using the Pythagorean trigonometric identity leads to:

$$k_{2;z}=k_{2;refracted}\sqrt{1-\sin^2\theta_2} \tag{2.7}$$

Finally, by inserting eq. 2.4 for θ_2 this leads straightforward to the following equation for $k_{2;z}$:

$$k_{2;z}=k_{2;refracted}\sqrt{1-\frac{n_1^2}{n_2^2}\sin^2\theta_1} \tag{2.8}$$

If $(n_1^2/n_2^2)\sin^2\theta_1>1$, which is the case for $\theta_1 > \theta_c$ (cf. eq. 2.4 and 2.5), the expression under the radical sign will become negative. Therefore, $k_{2;z}$ will be imaginary which states the existence of an evanescent wave in z-direction in accordance with eq. 2.3.

It is, however, necessary to note that TIRFM does not lead to a higher lateral resolution as the detected fluorescence signal is still a widefield signal. Much more important is the higher image contrast when the cell background is not excited any more. Fig. 2.7 demonstrates the effect of TIRF illumination: on the left, a classical widefield image of a labelled cell is shown, whereas the right one pictures the corresponding TIRFM image. The decrease of background combined with a higher contrast and Signal-to-Noise-Ratio (SNR) is apparent:

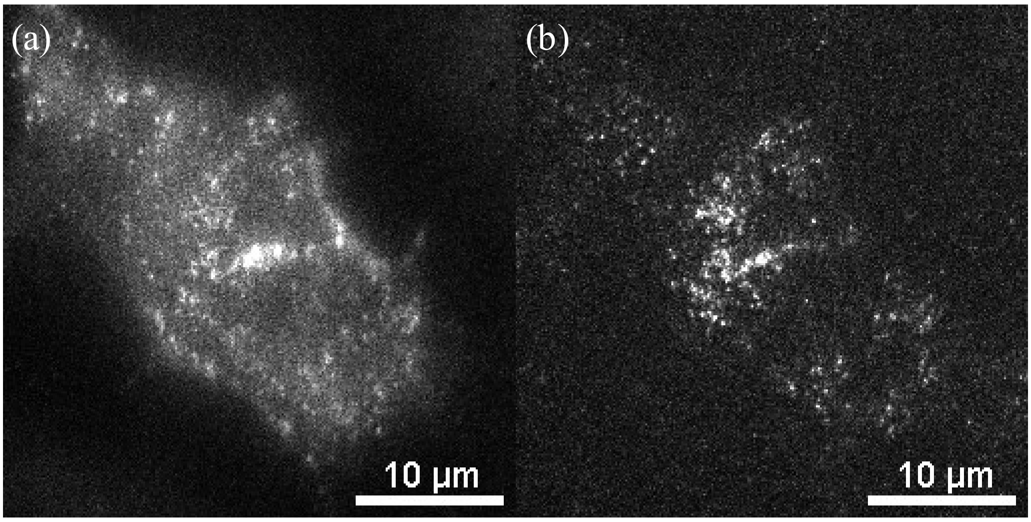

FIGURE 2.7: COMPARISON OF WIDEFIELD (a) AND TIRF ILLUMINATION (b) AT A SAMPLE OF FIXED HELA CELLS TRANSFECTED WITH A FLUORESCENT PROTEIN CONSTRUCT (λ_{EXC} = 561 nm)

After discussing the theoretical background, it is necessary to regard appropriate instrument configurations in order to realise TIRFM. In general, there are two main approaches for this purpose which will be explained with the help of fig. 2.8:

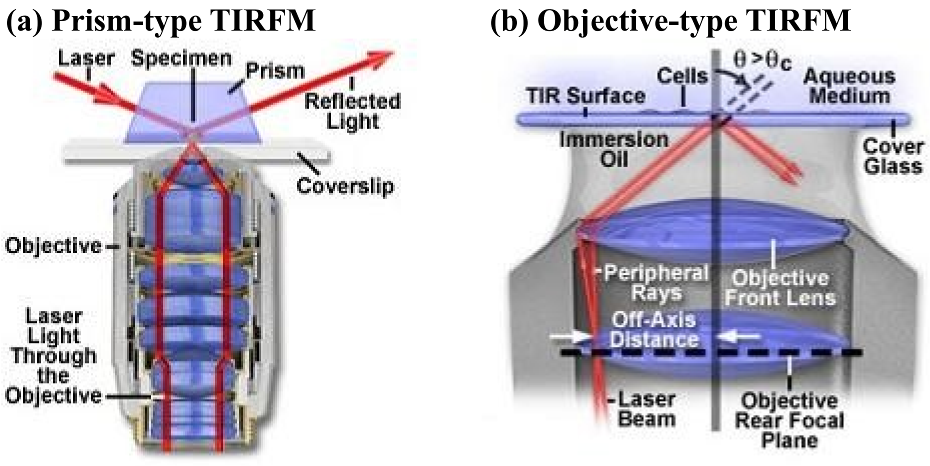
(a) Prism-type TIRFM
Laser
Specimen
Prism
Reflected Light
Coverslip
Objective
Laser Light Through the Objective
(b) Objective-type TIRFM
θ > θc
Cells
Aqueous Medium
TIR Surface
Immersion Oil
Cover Glass
Peripheral Rays
Objective Front Lens
Off-Axis Distance
Laser Beam
Objective Rear Focal Plane

Figure 2.8: Different illumination configurations for TIRFM: prism -type TIRFM (a) and objective-type TIRFM (b), taken from [15]

The first and older concept is called prism-type TIRFM and is demonstrated in fig. 2.8a. Here, the incoming laser beam is directed into a glass prism at an angle that exceeds the critical angle. Thus, the evanescent field is generated on one of the outer surfaces. Usually, the lower side is chosen, so that the coverslip with the sample can be placed beneath this surface and the resulting fluorescence signal can be detected by an objective on the other side of the coverslip, which means an inverted microscope configuration. But here also lies the main disadvantage of prism-type TIRFM: the inverted microscope requires detection of the fluorescence signal through the coverslip and the bulk of the sample. Furthermore, the access to the sample is restricted by this instrumental configuration.

For this reason, TIRFM was not widely accepted until the objective-type method was established to handle this problem. Here, the incoming beam is focussed on the back focal plane of the objective (fig. 2.8b), so that a collimated beam leaves the objective. When the beam is now delocalized from the centre of the objective, the collimated beam will leave the objective under a certain angle which will become larger with increasing off-axis distance. However, in order to allow angles large enough to achieve total internal reflection, objectives with high numerical apertures (≥ 1.40) are required.

2.4 Super-resolution Fluorescence Microscopy by STORM and PALM

2.4.1 General principle

In order to be able to take advantage of all the benefits fluorescence microscopy promises, it was an important challenge not only to increase imaging contrast by methods like TIRFM but also to find ways to surpass the diffraction limit that restricts many possible applications of this powerful tool. This task has been mastered by several methods which can be summarised by the term 'Super-Resolution Fluorescence Microscopy'. The basic idea of this concept lies in the fact that even when two spots, whose distance is smaller than the diffraction limit, cannot be resolved, the accuracy with which the position of a single fluorophore can be determined lies several orders of magnitude higher. How this fact can be used for super-resolution microscopy will be demonstrated with the help of fig. 2.9:

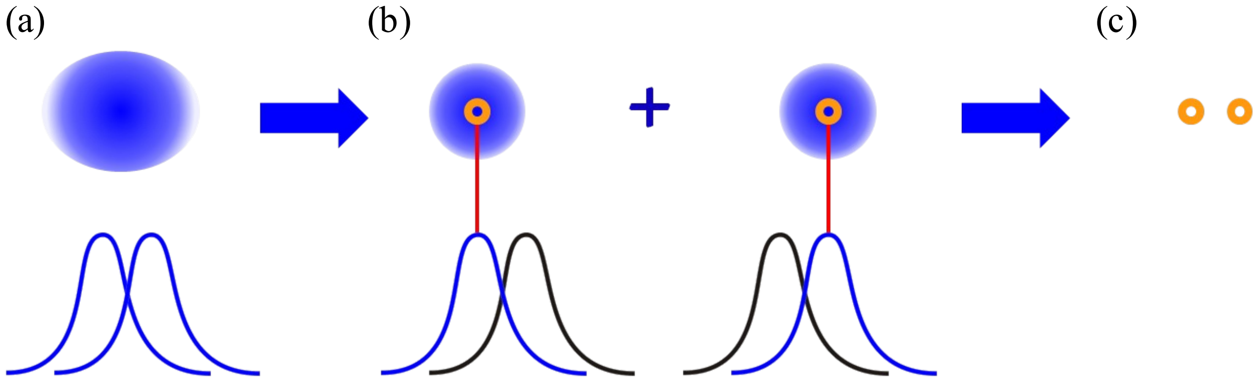

Figure 2.9: Principle of Super-Resolution Fluorescence Microscopy: (a) classical widefield image with two sample fluorophores both active, (b) both fluorophores are activated (blue) and deactivated (black) subsequently and the positions of the maxima of their PSFs are determined (c) combination of localized positions gives high-resolution image

At the beginning, there are two active fluorophores in a diffraction-limit spot. Therefore, there PSF will interfere and only a merged signal will be visible (fig.2.9a). If it was possible that there would be only one active fluorescent molecule as shown in fig.2.9b, it would be possible to determine its position with a very high accuracy by calculating the centroid position of the respective PSF. In the next step, the localized fluorophore would be switched off and the second one is activated and analysed in the same way. In the end, the combination of the localized positions would result in a high-resolution image (fig.2.9c) In this case, a resolution up to 20-30 nm [8] could be achieved what would mean an improvement of a factor of 10 compared to the usually achievable resolution of 200-300 nm [8] in classical optical microscopy.

Based on this principle, appropriate experiments can be designed. Two of them will be applied during the course of this study. Both were presented in 2006 for the first time: The first one was described by Rist, Bates and Zhuang [16] who called their experiment *Stochastic Optical Reconstruction Microscopy* (STORM); the other one is called *Photoactivated Localization Microscopy* (PALM) and was developed by Betzig *et al.* [17].

2.4.2 Stochastic Optical Reconstruction Microscopy (STORM)

Fig. 2.10 shows a schematic of a typical STORM experiment. A hypothetical sample is assumed, which has been labelled with a certain number of fluorophores which can be switched between a dark and a fluorescing state where they absorb light of the red part of the electromagnetic spectrum. Furthermore, the activation process will be induced by irradiation with green light.

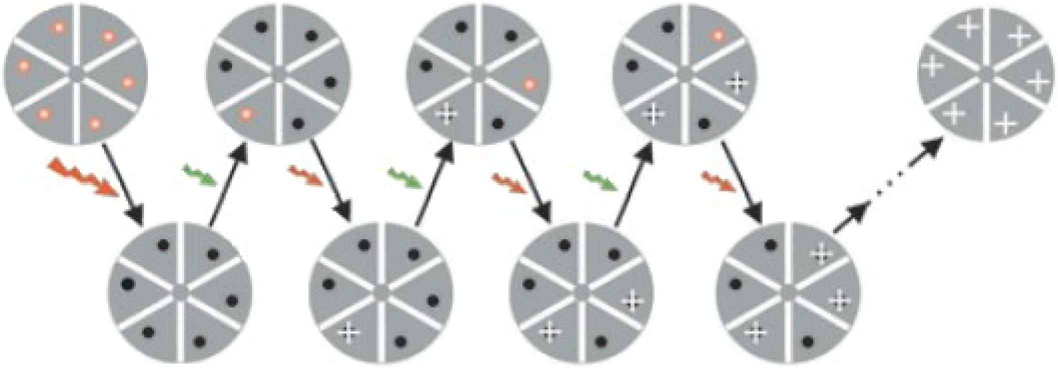

FIGURE 2.10: SCHEMATIC DEMONSTRATION OF A STORM EXPERIMENT, TAKEN FROM [16]
(RED: ACTIVATED FLUOROPHORE; BLACK: NON-ACTIVATED FLUOROPHORE; MARKED WITH CROSS: POSITION DETERMINED)

In the first step, the fluorophores are exposured to a strong red laser pulse, so that as many fluorophore as possible are deactivated (transferred to the dark state). In the following, the sample is irradiated with a green laser pulse that stochastically transfers a part of the fluorophores to the active state. Here, it is important that the power of the activating laser is not set too high because otherwise the probability increases that multiple fluorophores are activated within a diffraction-limited spot. This would lead to a loss of image quality and resolution because signals of the different PSF will start to interfere with one another.

The positions of the activated fluorophores can now be read with the help of the red laser. After a certain period of time, the molecules are deactivated again whereon another green laser pulse can stochastically activate other fluorophores. In this context, the power of the reading laser should be as high as possible in order to deactivate the fluorophores before the next activation pulse. These steps are now repeated as many times until an approximately complete image composed of the positions of all the fluorophores localized in all the steps before can be expected. For this purpose, up to 1,000 cycles can be typically necessary.

When a sufficient number of cycles of activation and deactivation has been performed, the image of the sample can be reconstructed with the help of the acquired data assuming that each activated fluorophore can be assigned to a three-dimensional PSF as shown in fig. 2.11a:

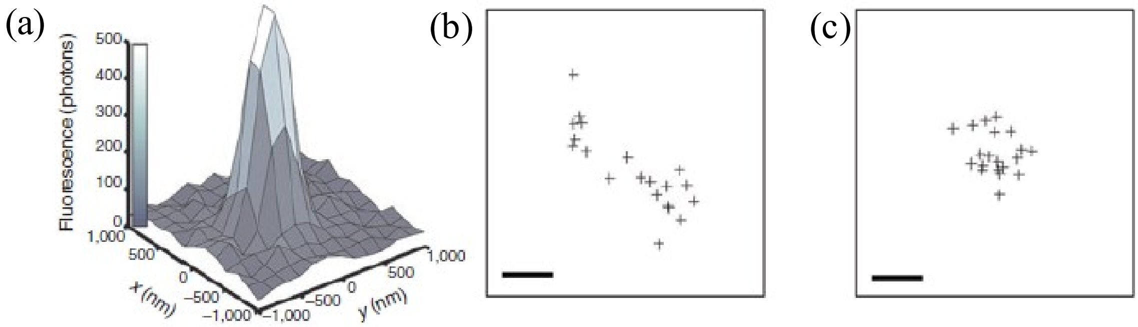

Figure 2.11: (a) Point spread function in three-dimensional space, (b) fitted centroids of PSF, (c) fitted centroids of PSF corrected for drift, taken from [16]

There are several methods (see also section 3.3) to determine the position of the PSF, the most common is fitting the PSF to a 2D Gaussian function, whose maximum yields the centroid of the PSF. The combined positions of all those centroids finally result in the reconstructed picture shown in fig. 2.11b. However, it might be possible, that a drift of the sample occurs during data acquisition. In this case, the obtained positions have to be corrected by this drift (fig. 2.11c) in order to get a realistic picture.

For STORM, photoactivation and deactivation are achieved by using photoswitchable organic dyes that can be switched reversibly between a fluorescent and a dark state. In [16], cyanine dye Cy5 (for spectral characteristics of the organic dyes used in this thesis, cf. table 5.2) was used for this purpose, but several other dyes are known that are suitable as well. Besides a various number of cyanine dyes, which are most common for STORM, also other photoswitchable dyes like photochromic rhodamine or caged dyes can be used [18].
When studying the switching process of different cyanine fluorophores, M. Bates *et al.* [19] discovered that activation efficiency of the observed fluorophore (reporter) is best when there is another dye molecule (activator) in a very close proximity (distance ≤ 10 nm) and when this dye has an absorption maximum at a lower wavelength than the reporter dye. For example, this effect was first shown in [19] using Cy3 and Cy5 as dye-pair where Cy3 is the activator and Cy5 the

reporter dye. Fig. 2.12 visualizes this activator-reporter interaction showing one exemplary deactivation and activation step. Deactivation takes place by irradiating the reporter with a high power laser pulse at a wavelength where the dye can be excited at its best. Activation is subsequently done by exciting the activator with a suitable laser pulse and, as mentioned above, it is recommended to use a low power pulse for activation in order to avoid multiple activations:

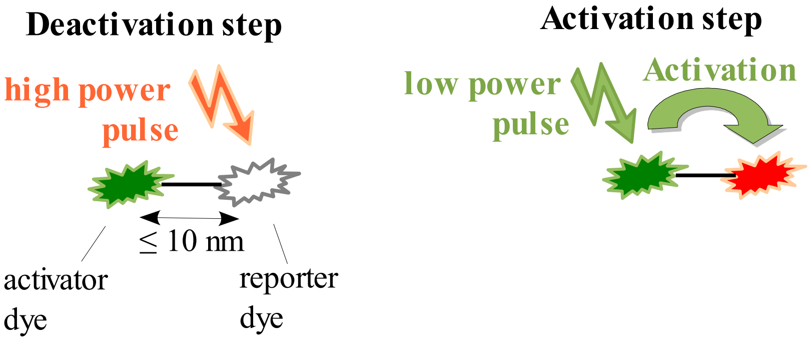

FIGURE 2.12: ACTIVATOR-REPORTER PRINCIPLE FOR STORM

Nevertheless, Sauer *et al.* showed that activation of the reporter dye is also possible at the same activation wavelengths as above when there is no activator dye present and called this variant of STORM 'direct STORM' (dSTORM) [20]. This method has the advantage that it is not necessary to put two different dyes in close proximity to each other, what is often difficult to achieve in the labelling experiment. In contrast, higher activation powers are required and the activation is less specific. Furthermore, the high activation specificity that can be achieved when using an activator-reporter system is also a big advantage of STORM when it comes to multi-colour applications: Two different structures can be labelled with the same reporter dye but with different activator dyes. Therefore, it is possible to activate the reporter dyes of each structure separately from each other. Alternatively, two- or multi-colour-STORM can also be realised by using the same activator and different reporter dyes; however, the first method has to be regarded as the preferred one because of the possibility of selective activation.

However, the mechanism of this activation process of cyanine dyes has not been explained satisfactorily so far. It is assumed that an energy transfer from the activator to a non-fluorescent state of the reporter could be responsible but there has been now proof for this theory until now. However, this process must follow other rules than common Förster Resonance Energy Transfer as a much steeper distance dependence is observed [19].

Also, the detailed nature of the dark state could not be explained definitely so far. It was suggested that the dye must undergo an intersystem crossing [19] in order to switch to the dark state as no switching can be observed in the presence of oxygen which, as a good triplet state

quencher, enhances the conversion from the triplet state back to the singlet state and therefore inhibits the switching. For this reason and also in order to reduce photobleaching, all STORM experiments have to be performed under an oxygen scavenging buffer (cf. methods section).
Another key for understanding the switching behaviour could be the fact that a reducing agent in form of a primary thiol (e.g. Cysteinamin or Mercaptoethanol) is required in order to observe deactivation. For example, Dempsey *et al.* [21] proposed a covalent binding of these thiol reagents on the polymethine system of the cyanine dye (cf. fig. 2.13). Thereby, the conjugated π-electron-system is interrupted and the absorption maximum is shifted to the UV range.

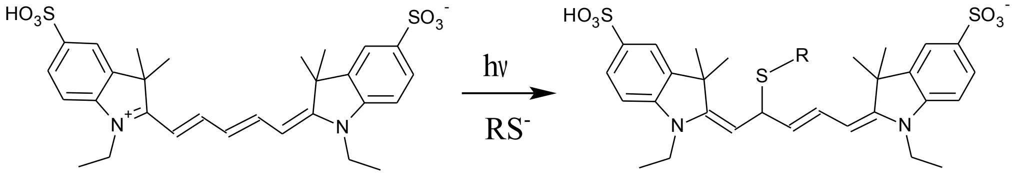

FIGURE 2.13: PROPOSED MODEL OF DARK STATE (AT THE EXAMPLE OF CY5), TAKEN FROM [21]

On the one hand, the reaction product could be detected by mass spectroscopy hence proving its existence. On the other hand, it remains unclear how this model fits with the activation of cyanine dyes supported by an other cyanine dye. For example, Cy5 can be activated with Cy2 as shown above but the product in fig. 2.13 only absorbs in the UV region. Therefore, it is difficult to understand how the required energy transfer should work. In the same work, a radical intermediate in the reaction pathway towards the product in fig. 2.13 was suggested and it might also be possible that this radical intermediate is the dark state observed in STORM experiments. This theory is also supported by the fact that the presence of a radical quencher like isoascorbate reduces switching rate to the dark state dramatically.

2.4.3 Photoactivated Localization Microscopy (PALM)

The principle of PALM, the second super-resolution microscopy method discussed in this work, is quite similar to STORM with regard to the procedure described on the basis of fig. 2.10. The main difference lies in the nature of the observed fluorophore: while in STORM, one generally uses photoswitchable organic dyes, PALM is based on the switching of photoactivable fluorescent proteins.

Luminescence and fluorescence are quite common phenomena in nature, a fact that has been well known for a very long time, but it was up to O. Shimomura, M. Chalfie and R. Tsien to demonstrate the usefulness of fluorescent proteins as an extremely powerful tool for biological research. In 1961, Shimonura was the first to extract and characterize a fluorescent protein, the so called Green Fluorescent Protein (GFP) from the jellyfish *Aequorea victoria* [22] while Chalfie and Tsien found similar species and developed numerous derivatives derived from these wild-type proteins, so that they were able to extend the colour palette to a wide spectrum [23]. All three scientists were finally honoured for their seminal work on this field with the Nobel Prize in Chemistry in 2008.

Later it was discovered that several fluorescent proteins show a photoswitchable behaviour: due to conformational changes or breaking of chemical bonds initiated by radiation with a certain wavelength, they can switch from a dark to an activated state or their absorption and emission spectra can shift. This switch can be reversible but especially when it is caused by bond breaking, it is irreversible. One example for these photoswitchable proteins that will be used for PALM in this work is EosFP which originates from the stone coral *Lobophyllia hemprichii* and which was first characterized by Wiedenmann *et al.* in [24]. The used form of EosFP shows a strong green emission with a maximum at 516 nm and a maximal absorbance peak at 506 nm until it is irradiated with UV-light with a wavelength in the range of 390 nm (cf. fig. 2.14). Then, the emission maximum changes to 581 nm in the red part of the electromagnetic spectrum and a new absorbance peak occurs at 571 nm. The switch of EosFP is irreversible and the converted protein will henceforth only emit red light until photobleaching occurs.

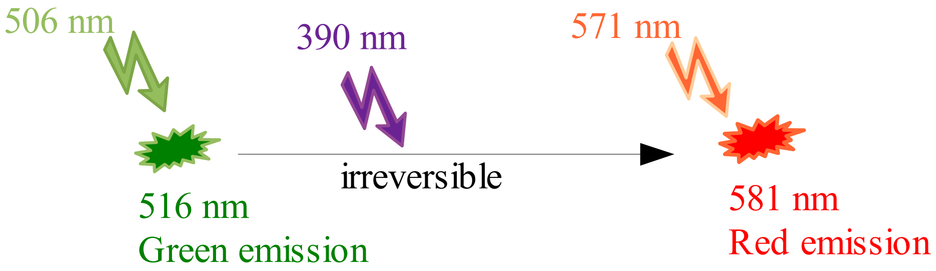

FIGURE 2.14: SWITCHING OF EOSFP

This fact shows one main advantage of PALM compared to STORM: As activation is not followed by deactivation but by permanent bleaching, each fluorophore is only activated once. From this follows that each observed signal can be assigned to one specific molecule. In contrast, a photoswitchable dye in STORM can be activated and deactivated several times, so if at a later point of time of a measurement, a signal is observed whose position is close to one of an earlier signal, it is often difficult to decide if there are actually two separate dye molecules or if both signals arise from the same molecule considering localization errors.

On the other hand, there are cases where PALM is not applicable: e.g. tagging a biological sample to a fluorescent protein can result in dominant-negative forms that might block the interactions that were originally intended to be studied. Also PALM depends on expression efficiency of these proteins that might be weak due to the large DNA constructs required for transfection. In these cases, STORM has to be used, which can be characterized by a wider field of application. But of course, it is also possible to do multicolour experiments by combination of a STORM and a PALM-system, e.g. by using an activator/reporter pair for STORM and a photoactivable protein for PALM on the other hand.

3 STORM and PALM imaging - measurement methods and analysis

3.1 Setup

3.1.1 Configuration

In this study, a homebuilt TIRF-widefield setup was used that was mounted onto an optical table. A schematic of the setup is shown in fig. 3.1:

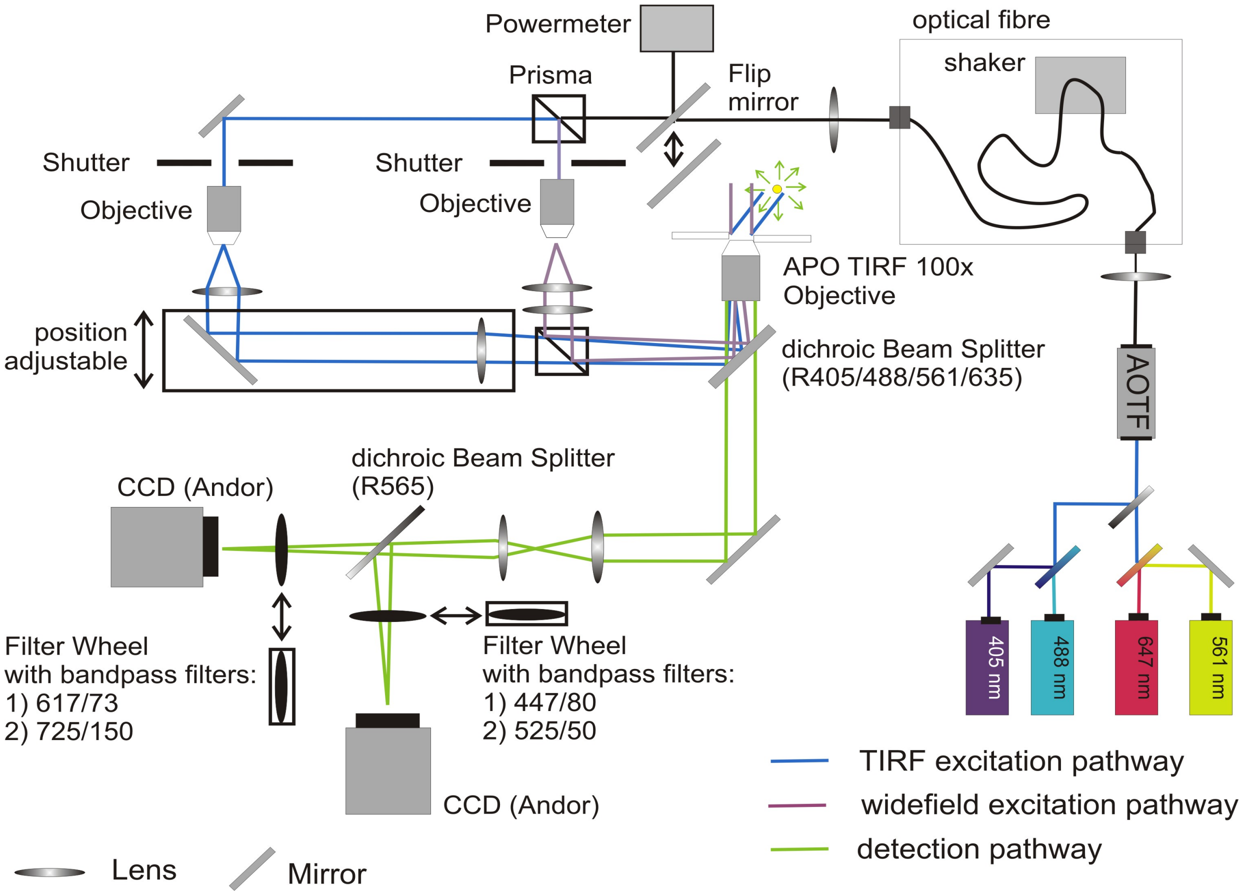
Powermeter
optical fibre
shaker
Prisma
Flip mirror
Shutter
Shutter
Objective
Objective
APO TIRF 100x Objective
position adjustable
dichroic Beam Splitter (R405/488/561/635)
AOTF
dichroic Beam Splitter (R565)
CCD (Andor)
Filter Wheel with bandpass filters:
1) 617/73
2) 725/150
Filter Wheel with bandpass filters:
1) 447/80
2) 525/50
CCD (Andor)
405 nm
488 nm
647 nm
561 nm
TIRF excitation pathway
widefield excitation pathway
detection pathway
Lens
Mirror

FIGURE 3.1: SCHEME OF THE EXPERIMENTAL SETUP

The lasers that were used as light sources are listed in table 3.1:

TABLE 3.1: LIST OF LASERS INSTALLED IN THE SETUP

Specification	Emitted wavelength
Coherent CUBE 405	405 nm
Picarro 20 mW Cyan Laser	488 nm
Crysta Laser	561 nm
Omicron PhoxX 642	642 nm

The different laser beams are aligned by dichroic mirrors before passing an Acousto-Optic Tunable Filter (AOTF) (AOTFnC-400.650, Quanta Tech) allowing to select distinct wavelengths and powers by modulating frequency and power of the AOTF. Then, the selected beam is coupled into a multimode optical fibre (diameter 200 µm, AMS Technologies) which was permanently shaken in order to prevent interference spots due to different possible pathways of the laser beam through the fibre.

After the fibre, a switchable mirror allows measurement of the laser power at this position in the excitation pathway (cf. fig 3.1). All power values given in this thesis were measured at this point if not specified otherwise. The beam is now separated by a prism in order to create two different pathways for widefield and TIRF excitation. Both can be controlled by opening and closing of shutters installed in the respective pathways.

The widefield beam is expanded by an objective-lens combination and then directly focussed on the centre of the back focal plane of the microscope objective (Nikon Apo TIRF 100x oil immersion objective, NA = 1.49) by a second lens. After this lens, the beam passes a second prism (for recombining the TIRF and widefield excitation pathways) before entering the microscope stage (Nikon Eclipse Ti) where the excitation beam is reflected into the objective by a dichroic mirror (R405/488/561/635). The main task of the dichroic mirror is the separation of excitation and detection beam. As the beam is focused on the back focal plane of the objective, the excitation beam leaving the objective will be collimated when the beam is focused on the centre of the objective, the resulting beam will leave the objective along the optical axis therefore resulting in widefield excitation.

The construction of the TIRF excitation pathway is similar to that of the widefield setup with the exception that the position of the last mirror before entering the microscope stage is adjustable in order to change the off-axis-distance of the focus in the back focal plane. The collimated beam will now leave the objective under a certain angle determined by the magnitude of the off-axis distance. When this angle is set large enough to exceed the critical angle (cf. theoretical section), TIRFM can be realised.

The fluorescence emission – after being separated by the dichroic mirror mentioned above, is guided out of the microscope stage and is divided into two beams by another dichroic mirror (R565) thereby creating a “blue” and a “red” detection channel. In both channels, a set of bandpass filters is mounted on a filter wheel in order to allow selection of distinct detection wavelengths (447/80 or 525/50 for the blue channel resp. 617/73 or 725/150 for the red channel).

Both detection beams are focussed on an electron multiplying CCD Camera (Andor iXon^{EM}+, controlled by Andor iQ software, version 1.9) by a set of two lenses situated in front of the last dichroic mirror. The pixel size is 68 nm for both detection channels.

3.1.2 Calibration and mapping of EMCCD cameras

Reconstruction of high-resolution images requires the exact number of detected photons. This number can be obtained from calibration of the CCD camera, a procedure that converts counts into photons. Furthermore, the different spectral channels (cf. fig 3.1) are distorted differently by various types of aberrations. Correction of these artefacts is referred to as mapping between the channels and is also highly important in high-resolution imaging.

3.1.2.1 Image acquisition by EMCCD cameras

Fig. 3.2 shows the schematic of an electron multiplying CCD (EMCCD) camera:

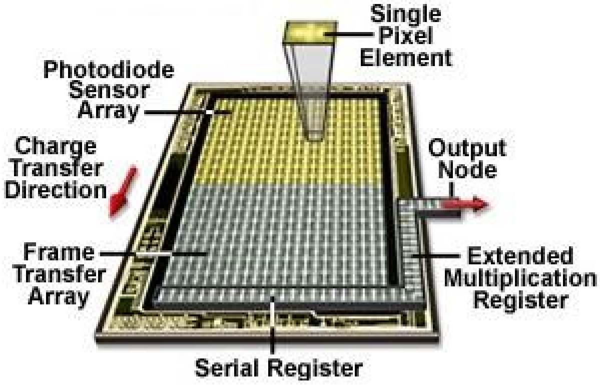

FIGURE 3.2: ELECTRON MULTIPLYING CCD ARCHITECTURE, TAKEN FROM [25]

The detection area is an array of photodiodes (shown in yellow in fig. 3.2) that have a certain finite size. When a photon impinges on one of these pixels, an electron-hole pair is generated. After exposure, the electrons are shifted to an opaque area of the array (shown in grey in fig. 3.2). This process is called frame-transfer and allows parallelized data acquisition and read-out, which results in a faster frame rate. The stored charges in the frame transfer array are now read out row by row by shifting to a serial register which sequentially shifts each row of the image to the output node. In an EMCCD, an extended multiplication register is placed between the serial register and the output node that is able to amplify the charge before reading. The resulting amplification factor is called 'Gain'.

The charge is then digitalized and subsequently assigned to a number of counts which in the end are depicted in the digital image. Summarizing, the number of photons N_p can be calculated by eq. 3.1:

$$N_P = \frac{(\text{Counts} - \text{camera offset}) * T}{\text{Gain}} \tag{3.1}$$

Here, T is the conversion factor which describes how many electrons are represented by one count in the digital image.

Due to this recording principle, the following noise sources must be regarded:

- ***Dark counts*** are created by spontaneous emission of electrons due to thermal excitation. This effect gets smaller when the temperature is decreased. When the camera is cooled to -90 °C, dark counts are about 0.002% electrons/pixel/sec and therefore negligible.
- ***Readout noise*** describes errors occurring during digitalization of charges, when the number of charges is changed in voltage. Readout noise is usually about 45 electrons per pixel; however, when using a EMCCD, this value changes to 45/Gain. The reduction of readout noise is the main advantage of EMCCDs as this error source can be considered as the resolution-limiting factor of standard CCDs assuming that the number of dark counts is low at low temperatures.
- ***Clock Induced Charge (CIC)*** describes single errors generated during charge transfer. CIC is usually smaller than readout noise, but in EMCCD CIC's are amplified as well (~ 1 event/line).
- ***Shot Noise*** arises from statistically fluctuations in the number of the detected photons and can be described by a Poissonian distribution. For a standard CCD, one can state that $\sigma_P^2 = N_P$, where σ_P^2 is the variance of the detected photons. For a EMCCD, an additional noise factor, called ***Multiplication Noise***, occurs as the gain factor is also subject to a distribution around a mean value. Therefore, the formula for the shot noise has to be corrected by a factor F which tends to $F = 2$ when the number of amplification steps is infinite and amplification probability for a single step is low [26]. Typically, for a 512x512 px camera, the amplification register contains 536 elements which can be considered a large number and F = 2. In this case, it can be stated that $\sigma_P^2 = 2 N_P$.

3.1.2.2 Camera calibration

If there were no other error sources than Shot Noise, it could be stated for the observed counts:

$$\frac{\sigma_C^2}{N_C}=\frac{\sigma_e^2}{N_e}=1 \tag{3.2}$$

Here, N_c and N_e are the number of camera counts and (multiplied) electrons and σ_c^2 and σ_e^2 the respective variances. But as there are also other, non-Poisson distributed noise factors, as described above, the actual ratio $(\sigma_e')^2 / N_e'$ is not equal 1. A correction factor called sensitivity S has to be introduced:

$$\frac{(\sigma_e')^2}{N_e'}=\frac{\sigma_e^2}{N_e}*S \tag{3.3}$$

which leads to the following expression for σ_c^2 / N_c:

$$\frac{\sigma_C^2}{N_C}=\frac{(\sigma_e')^2}{N_e'}=\frac{\sigma_e^2}{N_e}*S \tag{3.4}$$

and as $\sigma_e^2 / N_e=1$ (cf. eq. 3.2):

$$\frac{\sigma_C^2}{N_C}=S \quad \text{or} \quad \sigma_C^2=S*N_C \tag{3.5}$$

The sensitivity can be measured by plotting the variance of counts against the mean number of counts where the sensitivity will be the slope of the graph. For this purpose, an image stack sample of fluorescein labelled 2.0 µm sized polystyrene beads was measured (500 frames), the mean values and variances for all pixel coordinates over the whole image stack were calculated using a MatLab (R2009b from The MathWorks) script written for this purpose. Subsequently, the variances were plotted against the mean values and smoothed (cf. fig 3.3). The slope was determined by linear fitting of the data for the mean values between 0 and 4000 counts as only here the statistic appeared good enough to deliver reliable results:

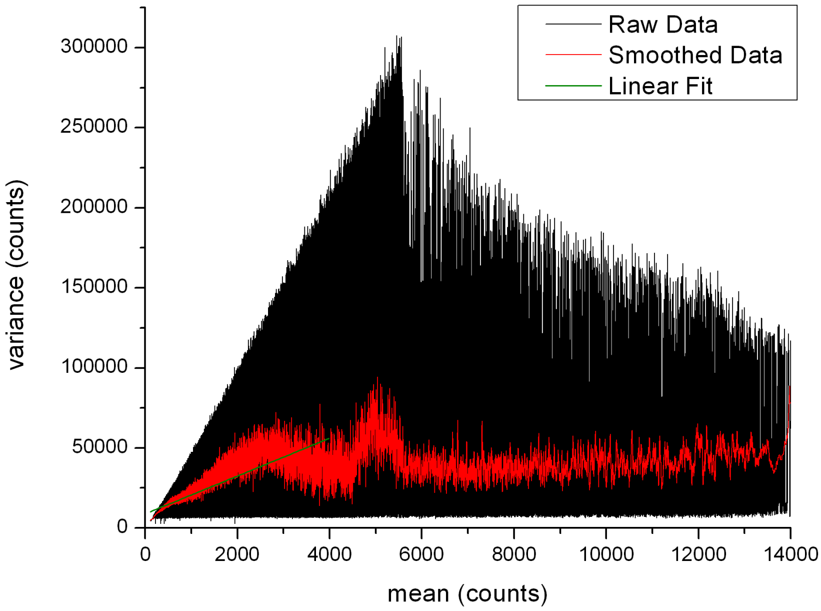

FIGURE 3.3: CAMERA CALIBRATION: VARIANCE OF COUNTS PLOTTED AGAINST MEAN VALUES OF COUNTS

Here, a sensitivity of 11.8 electrons/counts was calculated. This result agrees with the value determined by Andor Technical Service (sensitivity = 12.0 electrons/count).

However, as the sensitivity factor determined by this method only regards errors caused by analogue-to-digital conversion, eq. 3.1 must be modified to the expression given by eq. 3.6 in order to regard Multiplication noise:

$$N_P = \frac{(\text{Counts} - \text{camera offset}) * 2 * \text{Sensitity}}{\text{Gain}} \tag{3.6}$$

Therefore, the sensitivity has to be corrected by a factor of 2 when the actual number of photons is calculated. This result agrees with measurements performed by Stefan Wickels [27] (2 * Sensitivity ~ 20 electrons/count), where the sensitivity was determined by measuring the respective count rates for different gain settings. In contrast to the method used above, this approach already includes the noise coming from electron multiplying.

3.1.2.3 Camera mapping

The images obtained by two different cameras used in one system are not necessarily aligned completely as there can be a shift or distortion between the two detection channels. When both images are to be compared, it is necessary to correct this effect by mapping the cameras. The term 'mapping' describes the calculation of a transformation matrix that projects the coordinates obtained from the first camera on the corresponding image coordinates obtained from the second camera. Here, this transformation matrix was determined by solving the following third-order polynomial, also using a programme written in MatLab (R2009b from The MathWorks):

$$\begin{pmatrix} u \\ v \end{pmatrix} = (1\ x\ y\ xy\ x^2\ y^2\ yx^2\ xy^2\ x^3\ y^3) * T_{inv} \qquad (3.7)$$

T_{inv} is a 10x2 transformation matrix that projects the base coordinates x and y on the corresponding image coordinates u and v. For solving this third order polynomial, ten corresponding coordinate pairs from both images were required. For this reason, an image of a sample of 200 nm sized polystyrene beads, labelled with fluorescein was collected in both channels. Ten related points were then selected from both images and their coordinates used for the calculation of the transformation matrix. The result of this process can be seen in fig. 3.4. The left picture shows the composite of the images from both channels before mapping is done, while the right one depicts the corresponding picture after applying the transformation matrix.

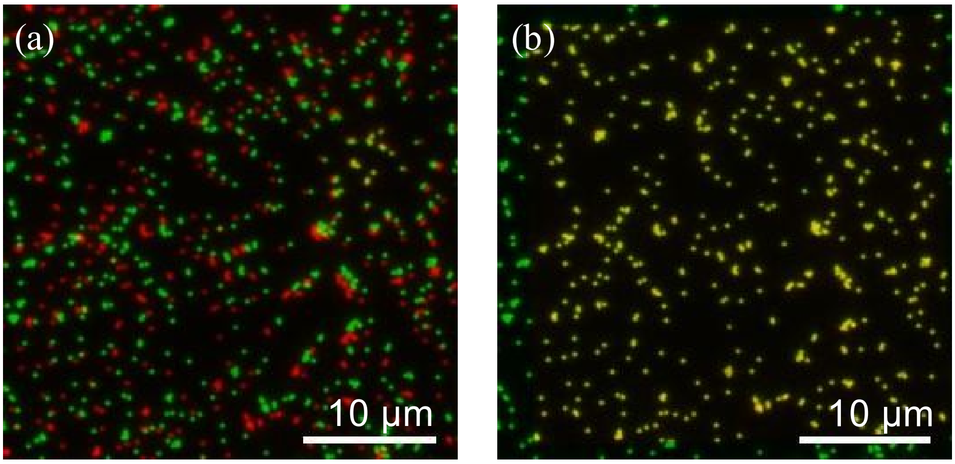

Figure 3.4: Camera mapping: (a) non-transformed image, (b) transformed image

The transformation matrix determined in this case is:

$$T_{inv} = \begin{pmatrix} 30.3019 & 23.2083 \\ 0.9091 & -0.0354 \\ 0.0173 & 0.9220 \\ 0 & 0 \\ 0 & 0.0001 \\ 0 & 0 \\ 0 & 0 \\ 0 & 0 \\ 0 & 0 \\ 0 & 0 \end{pmatrix} \qquad (3.8)$$

The good alignment of the points achieved in fig 3.4b demonstrates that camera mapping was successfully performed by using the calculated transformation matrix T_{inv}.

3.2 Optimization of measurement protocol

Although many studies have already been performed concerning the optimization of the ideal parameters under which STORM and PALM experiments can be performed at best (eg. [16]), there were still several adjustments to be made for our system. On the one hand, this implies finding the optimal setup settings, but especially when it comes to STORM, also environment conditions are critical for the the success of the experiment. Even small changes of these conditions can dramatically effect the activation and deactivation dynamics in STORM experiments. Therefore, several experiments on test systems described in the this section were performed in order to find the optimal parameters for the switching behaviour of the fluorophores.

3.2.1 Used test systems

The following samples were used as test systems for STORM experiments: The first experiments were performed with biotin coated polystyrene beads with a diameter of 200 nm. In order to label these beads with appropriate dyes for STORM, streptavidin was labelled with Cy2 as an activator and Alexa Fluor 647 as a reporter dye. These labelled proteins were given to the biotin coated beads to which they bind due to the strong intermolecular interactions between streptavidin and biotin. This system was used again in this study for finding optimal measurement conditions.

For testing the ability of the system to reproduce objects smaller than the Rayleigh criterion, the first measurements were performed with neutravidin coated polystyrene beads with a diameter of 40 nm which were labelled with the same dyes as above for the 200 nm beads. For the last step before being able to go on to a sample whose structure is unknown, it was necessary to test the method on a system with a complexer but well-known structure. For this purpose, microtubuli of HeLa cells were stained with anti-β-tubulin antibodies which were also labelled with Cy2 as an activator and Alexa Fluor 647 as a reporter dye.

3.2.2 Optimization of data acquisition protocol

The following measurement protocol was established for STORM and PALM measurements: The activation/deactivation cycles (respectively activation and bleaching for PALM) consisted of one activation pulse followed by 59 reading pulses. For each measurement, 5,000 to 25,000 image were taken. In general, shorter measurements do not allow a complete image reconstruction while longer measurements usually do not improve image quality significantly.
Laser power was set to 10 - 50 µW (measured after optical fibre, cf. fig. 3.1) for activation and to maximum power for reporting (~40 mW for $\lambda_{exc} = 642$ nm and ~15 mW for $\lambda_{exc} = 561$ nm). Activation power should be chosen as low as possible because otherwise multiple fluorophores may be activated in a diffraction-limited spot. In contrast, reading power should be chosen as high as possible in order to achieve deactivation before the next activation pulse.
The camera exposure time was set to a value of 50 ms resulting in a total frame rate of 55 ms/frame. Under these parameters, the activated fluorophores remain in the active state for a sufficient number of frames emitting enough photons for successful data evaluation before becoming deactivated again. The EM-Gain as set to a value of 500.

In this context, it is necessary to define the terms 'activation frame' and 'reporting frame'. The first expression stands for images taken at the respective excitation wavelength for activation and the latter for images taken at the respective excitation wavelength for imaging.

3.2.3 Optimization of measurement conditions for STORM

a) Oxygen exclusion

A crucial condition for STORM measurements is the complete exclusion of oxygen from the sample chamber. Therefore, all STORM experiments have to be performed using an oxygen scavenging buffer containing 8 % w/v glucose which is able to reduce the existing oxygen to hydrogen peroxide catalysed by glucose oxidase (0.5 mg/mL). In order to avoid chemical bleaching of the fluorophores, the produced hydrogen peroxide has to be degraded by catalase (10 µg/mL) according to the following reaction:

$$2\,H_2O_2 \longrightarrow 2\,H_2O + O_2$$

To prevent new oxygen from entering the sample chamber, special chamber slides with an increased wall thickness are used (LabTek II chamber slides from Thermo Fisher Scientific with a thickness of 0.16 – 0.19 mm). Other chamber slides like LabTek I (thickness 0.13 – 0.17 mm) from the same company have emerged as inappropriate [28] as diffusion of oxygen is too fast in this case. In order to achieve maximum measurement times, it is necessary to add the glucose to the STORM imaging buffer only immediately before the measurement and to seal the chamber with paraffin.

b) Reducing agent

As discussed in the theoretical section, a certain amount of reducing agent is required in order to achieve activation and deactivation of the dyes. In the original work by Rust *et al.*, β-Mercaptoethanol was used for this purpose but in [29], Huang *et al.* proposed to replace β-Mercaptoethanol by Cysteinamin (β-Mercaptoethylamin), which not only shows a better ability to reduce uncontrolled activation of fluorophores but can also be characterized by its significantly lower toxicity compared to β-Mercaptoethanol.

First experiments showed that it is not possible to deactivate the dyes effectively when the concentration of Cysteinamin in the buffer is too low. High excitation powers of the reporting laser and long deactivation cycles did not bring any improvement: instead of deactivation, only permanent bleaching could be observed. It was subsequently shown that a 50 mM solution of Cysteinamin is required in order to allow effective switching of the dyes to the dark state.

On the other hand, it should be kept in mind that Cysteinamin is not stable in aqueous solution. Even when stored at -80 °C, a precipitation of a colourless solid was observed after a few days. It is a assumed that a polymerization reaction occurs according to the mechanism depicted in fig. 3.5:

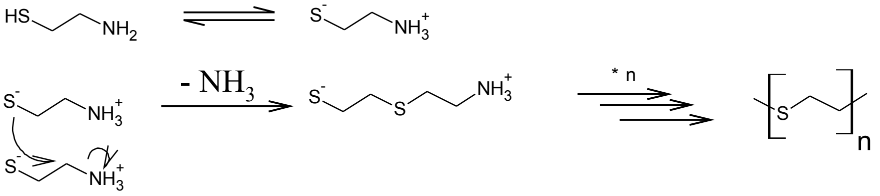

FIGURE 3.5: SUGGESTED MECHANISM FOR DEGRADATION OF CYSTEINAMIN BUFFER

This fact is supported by the observation that no precipitation occurs if Cysteinamin is stored in a solution of concentrated sodium hydroxide (pH = 14). The extremely high pH value protects the amino group from being protonated and therefore inhibits the reaction showed above. Additionally, β-Mercaptoethanol also does not show such a degradation, which can be explained by the fact that latter one is not equipped with an amino-group and is therefore unable to undergo the reaction above.

A further parameter that has to be taken into consideration is the pH value of the imaging buffer. In order to determine the optimal conditions, samples of 200 nm polystyrene beads were prepared as described in 3.2.1. They were subsequently measured under the same conditions at a constant laser power and the same buffer composition with the exception of the pH value. For this measurement, a relatively high activation power of 200 µW was chosen in order to be able to observe activation and deactivation kinetics. Multiple activations were desired to obtain good statistics this time; the results shown in figures 3.6 and 3.7 therefore represent ensemble measurements. After data acquisition, a representative bead was selected from each measurement. For this bead, the respective mean count rates were determined for all reporting frames as shown in fig. 3.6 at the example of the measurement performed at pH = 8. The graph shows the background corrected count rate of the reporting frames over a number of activation cycles. Activations are symbolized by red dashed lines. It can be stated that the observed intensity jumps to high values after each activation before slowly returning to the ground level as more and more of the activated fluorophores are becoming deactivated.

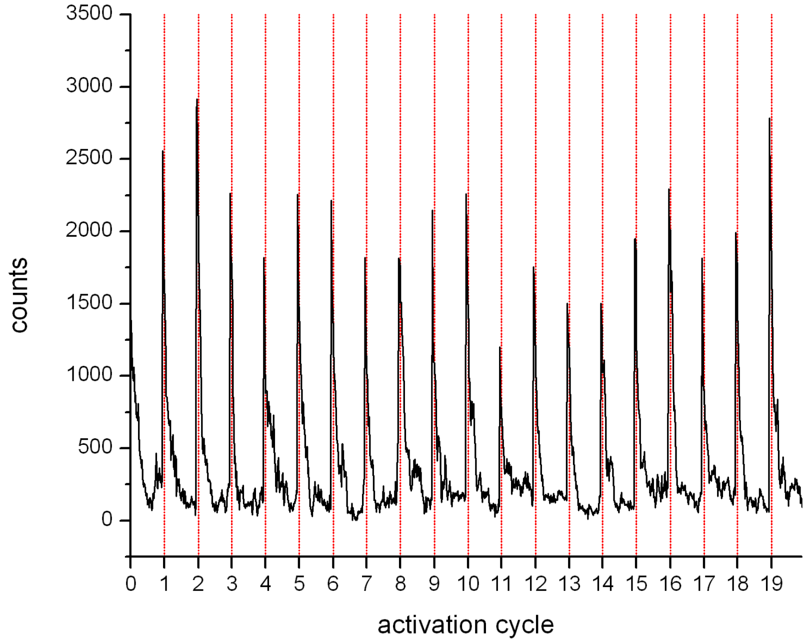

FIGURE 3.6: DEMONSTRATION OF ACTIVATION AND DEACTIVATION (BUFFER PH = 8)

Following, an average activation cycle was calculated for the different pH measurements by building the respective average values of the mean count rates of all the reporting frames coming first, second, third etc. after the activation pulse. The data obtained by this method (cf. fig. 3.7) should give a good idea about the magnitude of the activation rates as a higher average count rate observed at the beginning of the average cycle indicates a higher activation rate. The average number of frames until all the fluorophores are in the dark state again gives information about the deactivation rate.

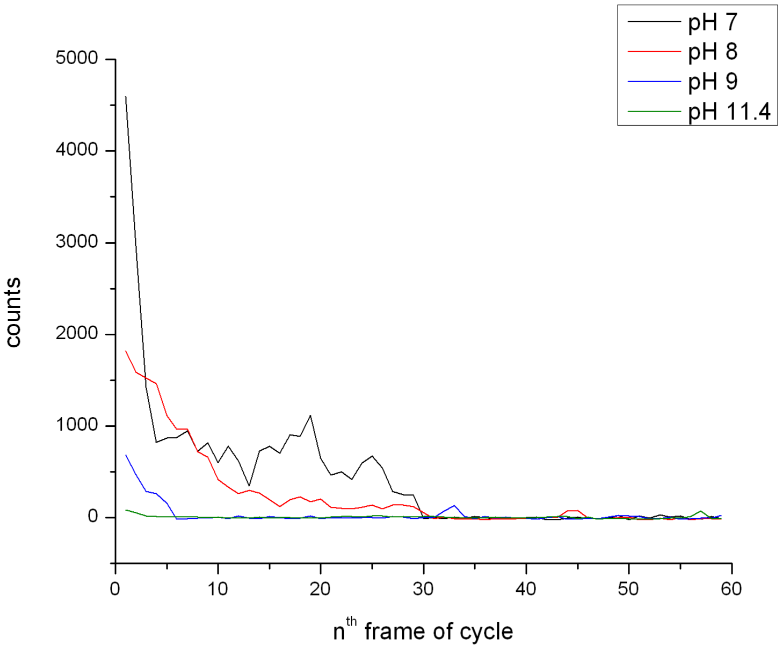

FIGURE 3.7: AVERAGED ACTIVATION CYCLE FOR DIFFERENT IMAGING BUFFER PH VALUES

Considering the data shown in fig. 3.7, it is clearly visible that low pH values result in a higher activation rate and slower deactivation. The obtained mean count rates subsequently drop with increasing pH until they approximately reach the level of background noise at pH = 11.4. Therefore, it can be stated that only poor activation is possible for pH ≥ 11.4. High pH values of the imaging buffer are obviously inappropriate for STORM measurements. On the other hand, the activation effectivity should also not be too high in order to avoid multiple activations and to ensure deactivation until the next activation pulse. Therefore, an imaging buffer equilibrated to pH = 8 was chosen for the measurements in this study, where the activation rates were in a medium range and therefore they should be able to act as a good compromise.

3.3 Image reconstruction

After optimization of sample preparation and data acquisition, the next step that has to be addressed is the reconstruction of the final image. When choosing the respective method, value has to be placed on the accuracy of the used method but it is also important that data evaluation can be performed in an adequate amount of time. Therefore, two different reconstruction methods – 2D Gaussian fitting and the non-fitting FluoroBancroft algorithm – will be tested during the course of this chapter and their results will be compared.

3.3.1 2D Gaussian Fitting

The most common way of STORM and PALM image reconstruction is fitting the obtained data to a two-dimensional Gaussian function. Although the PSF has not exactly the shape of a Gaussian function, it is a good approximation [30]. The programme for this purpose is based on the procedure described by Rist, Bates and Zhuang [16] and was written by Volodymyr Kudryavtsev in LabView 2009 (v 9.0, National Instruments) and further developed during the course of this study.

Starting from the raw data, an intensity threshold is applied to each frame of the image stack in order to find signals suitable for evaluation. These events were subsequently localized by least-square fitting using a two-dimensional elliptical Gaussian function, which is given at the position (x, y) as follows:

$$I(x,y)=A+I_0 e^{\left[-\left(\frac{(x-x_0)\cos\theta-(y-y_0)\sin\theta}{\sigma_x}\right)^2-\left(\frac{(x-x_0)\sin\theta-(y-y_0)\cos\theta}{\sigma_y}\right)^2\right]/2} \tag{3.9}$$

where x_0 and y_0 stand for the centre coordinates of the peak, A is the intensity of the fluorescing background, I_0 the amplitude of the signal, σ_x and σ_y the standard deviations of the Gaussian distribution in x- and y-direction respectively and θ the tilt angle of the ellipse relative to the pixel edges. The fit parameters are listed in table 3.2 along with their respective initial values:

Table 3.2: Fit parameters and Initial vlaues for Gaussian Fitting

parameter	initial value
x_0, y_0	coordinates of brightest pixel in this event

I_0	intensity of brightest pixel in this event
θ	1 rad
σ_x, σ_y	1 px
A	mean of count distribution of a representative crop without events in this frame

The maximum number of iterations was set to 50. After the fitting process was finished, the final image was reconstructed from the centroid positions of the fitted Gaussian curves. Peaks with a too high ellipticity were rejected as such spots are most likely due to more than one activated fluorophore at this place whose signals may interfere with one another and therefore affect image quality. The ellipticity is defined as:

$$E=\left|2(\sigma_x-\sigma_y)/(\sigma_x+\sigma_y)\right| \tag{3.10}$$

In this work, ellipses with E > 0.15 were discarded.

In addition to the ellipticity threshold, another criterion was implemented into the programme that considers errors due to photon noise, background noise and the finite size of the pixels. A formula summarizing all these three contributions was presented by Thompson *et al.* [31], where the standard error of the mean $\langle(\Delta x^2)\rangle$ is given by:

$$\langle(\Delta x^2)\rangle=\frac{\sigma^2}{N}+\frac{a^2/12}{N}+\frac{4\sqrt{\pi}\,\sigma^3 b^2}{N^2} \tag{3.11}$$

Here, the first addend represents the error caused by photon noise where N is the number of photons collected and σ the standard deviation of the fitted PSF where it is assumed that $\sigma = \sigma_x = \sigma_y$. In the second term, a stands for the finite size of the pixel and the third part of the formula represents the error caused by the background noise b.

The applicability of this method for single molecule localization was shown by Cronin *et al.* [32], demonstrating that if all localized events with an error $\Delta x=\sqrt{\langle(\Delta x)^2\rangle}$ greater than 10 nm are discarded, this will lead to an improvement of image quality. So – if not said otherwise – this criterion was applied to all evaluations in this work. All other events were added to the final image in form of two dimensional Gaussians defined by eq. 3.12, using an intensity I_0 of 1000 counts and a standard deviation σ of 1.25 px. x_0 and y_0 are the centroid coordinates obtained from the fitting.

$$I(x,y)=I_0*\exp\left[-\frac{(x-x_0)^2+(y-y_0)^2}{2\sigma^2}\right] \tag{3.12}$$

The following pictures show examples of the evaluation of data obtained from the different test systems described above. First, a sample of 40 nm sized polystyrene beads (labelled with Cy2 and Alexa Fluor 647) was measured with the settings described in 3.2.2. The result of the subsequent reconstruction is shown in the fig. 3.8:

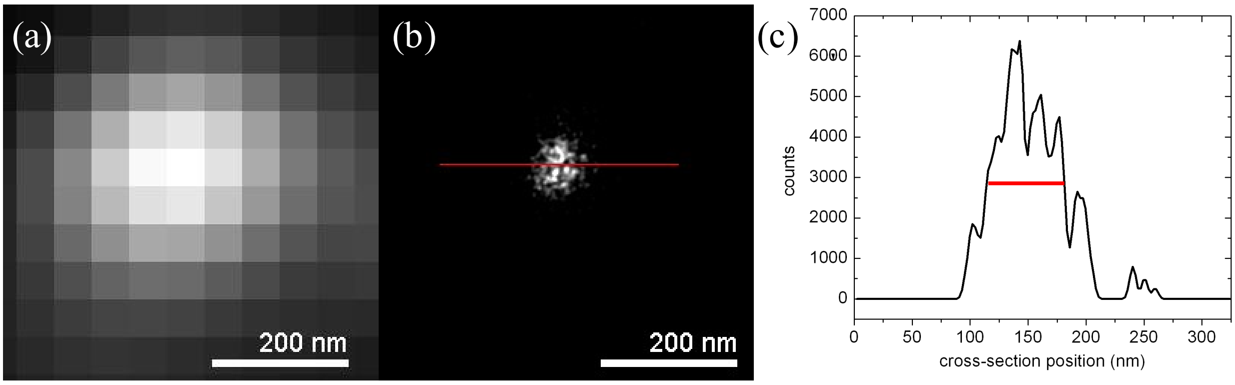

Figure 3.8: Example for STORM image evaluation: neutravidin coated 40 nm polystyrene bead labelled with Cy2/Alexa Fluor 647 (a) average projection of reporting frames, (b) STORM image of a), (c) Cross-sectional distribution of localizations generated from the data marked in b). The red line shows a FWHM of 59 nm

Fig. 3.8a shows the original raw data as an average projection over all reporting frames. In fig. 3.8b, the reconstructed STORM image is presented. This example nicely illustrates the resolution gained by STORM. While in classical microscopy the small size of the bead cannot reproduced correctly, the STORM image goes beyond this limit. The form of the spherical bead is clearly visible and also the size is reproduced in an adequate range (~ 60 nm at FWHM of the corss-sectional profile shown in fig. 3.8c although the bead appears to be larger than it really is. However, this is an observation that has been made in almost all the studies dealing with STORM (e.g. [20]). This phenomenon can be explained by the finite size of the proteins that were used for sample labelling and contribute to the measured size of the sample, e.g. when the protein is binding on the very edge of the sample.

After the successful reconstruction of small beads, we proceeded to a complexer system. The microtubuli of HeLa cells were stained with Cy2 and Alexa Fluor 647 labelled anti-β-tubulin antibodies. The results of this experiment are summarized in figure 3.9:

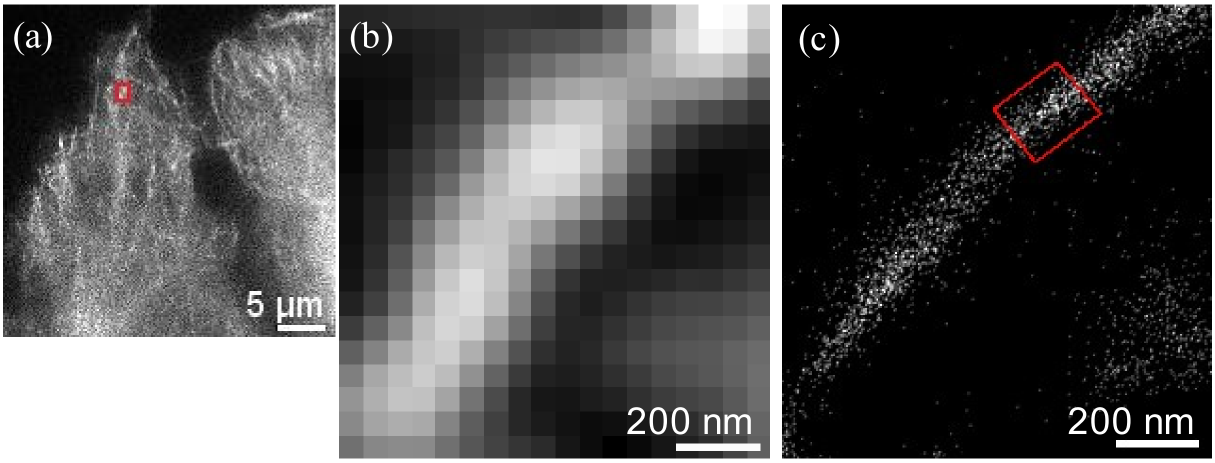

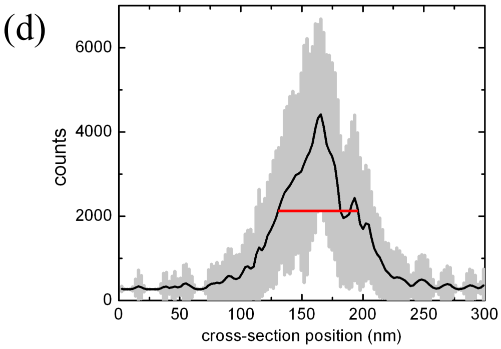

FIGURE 3.9: EXAMPLE FOR STORM IMAGE EVALUATION: HELA CELL LABELLED WITH β-TUBULIN ANTIBODIES LABELLED WITH CY2 AND ALEXA FLUOR 647: (a) WIDEFIELD ACTIVATION IMAGE, (b) PROJECTION OF REPORTING FRAMES FROM THE DATA MARKED IN a), (C) STORM IMAGE OF b), (D) CROSS-SECTIONAL DISTRIBUTION OF LOCALIZATIONS GENERATED FROM THE DATA MARKED IN c). THE RED LINE SHOWS A FWHM OF 65 NM (GREY: STANDARD DEVIATION)

The microtubuli image was reconstructed successfully with super-resolution. The gain in resolution is visible although the size of the microtubulus in fig. 3.9c still seems to be larger than it would be expected from literature. An average diameter of 65 nm was measured for this sample, whereas literature values state the size to be around 25 nm [33]. Similar to the argumentation for the beads, this observation can be explained by the finite size of the antibodies that were used for sample labelling. In order to reduce this effect, it is necessary to find appropriate antibodies that offer a small size and also a small fab-fragment (the region where the antibody is binding to the antigen). A solution might be to use fluorescent, antigen-binding nanobodies (chromobodies) that were introduced by Rothbauer *et al.* [34].

3.3.2 Non-fitting localization based on FluoroBancroft algorithm

Although 2D Gaussian fitting offers good results, this method is limited by relatively long calculation times. For example, the evaluation of a lager image (e.g. the sample in fig. 3.9a) can take up to several hours, depending on the number of fitting events and the processing power of the used computer system. However, fast image reconstruction is important when one desires to get reconstruction results immediately after measuring in order to judge the results of a measurement before performing time-consuming evaluations of non-optimal data.

One solution to speed up the process is to decrease the number of iterations for each fitting as it does not make sense to perform calculations with accuracies better than 10 nm. This value is the resolution limit for STORM and PALM as the magnitude of localization errors usually does not allow more accurate localizations. However, this reduction was insufficient for significantly improving the calculation speed.

Another approach to reduce calculation time would be to decrease the number of fitting parameters. Wolter, Sauer *et al.* presented an algorithm, where the standard deviations of the Gaussian, σ_x and σ_y, and the orientation, θ, were fixed. With this algorithm, they were able to speed up the process in a way that even real time reconstruction was possible [35]. Another variation was suggested by Smith *et al.* who used the Graphic Processing Unit (GPU) of the evaluation computer in combination with a maximum-likelihood-estimation which also gave excellent results concerning both localization accuracy and calculation time [36]. A third alternative is the so called FluoroBancroft algorithm [37][38] that surpasses the long calculation time by offering a completely analytical solution without fitting.

In this study, the FluoroBancroft algorithm, first presented by Andersson [37], was implemented as an appropriate alternative to 2D Gaussian fitting. This algorithm reveals an elegant way to determine the exact position of a single fluorescent emitter in a completely analytical way without the need of numerical fitting. Furthermore, Hedde, Nienhaus *et al.* were already able to show in [38], that this method is applicable for PALM, where an evaluation speed of a factor 100 higher compared to 2D Gaussian fitting could be achieved.

3.3.2.1 Principle of the FluoroBancroft algorithm

Assuming a 2D Gaussian distribution with a maximum amplitude I_0, a standard deviation σ and a background noise N_B the signal intensity I at the coordinates (x, y) is given by:

$$I(x,y)=I_0*\exp\left[-\frac{(x-x_0)^2+(y-y_0)^2}{2\sigma^2}\right]+N_B \tag{3.13}$$

When σ is known, this parameter gives information about the size of the Gaussian and therefore also about its steepness. If the intensity of a point on this Gaussian function $I(x, y)$ is taken (cf. fig. 3.10a), then this intensity value gives information on how far this 'control point' is away from the centroid position of the Gaussian distribution at (x_0, y_0). In that way, the distance r_i between the control point (x, y) and the centroid can be calculated. If this distance determination is performed for at least three different positions, (x_0, y_0) can be assigned unambiguously by Triangulation at the intersection of the circles around the respective control points with radii r_i. (cf. fig. 3.10b). This principle is analogous to the localization of an object on Earth surface via

GPS or the Nano Positioning System used for macromolecular structural analysis [39].

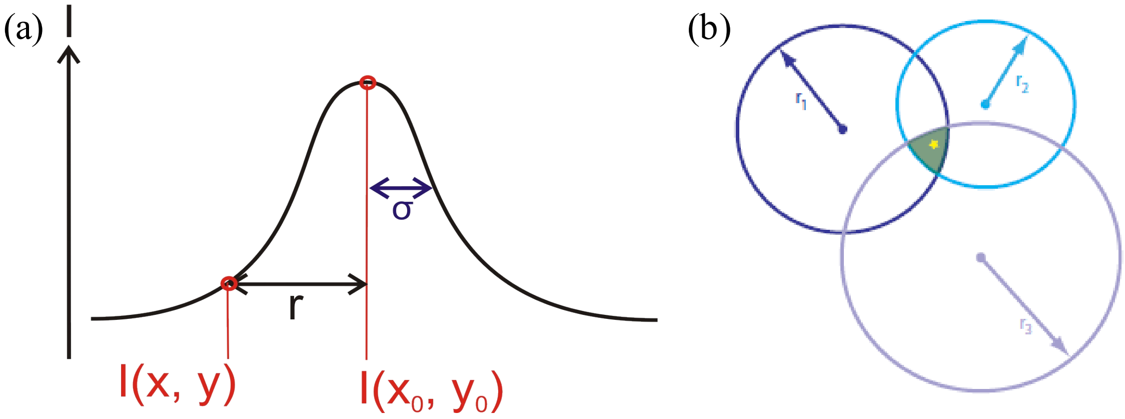

Figure 3.10: Principle of FluoroBancroft algorithm: (a) Determination of distance to centroid by using the steepness of the function, (b) Localization of a single emitter by triangulation (b taken from [37])

The detailed derivation of the solution of this problem is described in [37], where conclusively the analytical solution for the centroid of a Gaussian distribution defined by eq. 3.13 is given by:

$$\begin{pmatrix} x_0 \\ y_0 \end{pmatrix} = Q B^{+} \alpha \tag{3.14}$$

where Q is defined as

$$Q = \begin{pmatrix} 1 & 0 & 0 \\ 0 & 1 & 0 \end{pmatrix} \tag{3.15}$$

and B^{+} is the Moore-Penrose inverse (pseudo-inverse) of the following matrix B:

$$B = \begin{pmatrix} x_1 & y_1 & 1 \\ \vdots & \vdots & \vdots \\ x_n & y_n & 1 \end{pmatrix} \tag{3.16}$$

where (x_i, y_i) are the coordinates of the respective points for which the distance to (x_0, y_0) is calculated. Furthermore, α is given as:

$$\alpha = \begin{pmatrix} \frac{1}{2}(x_1^2 + y_1^2 + P_1^2) \\ \vdots \\ \frac{1}{2}(x_n^2 + y_n^2 + P_n^2) \end{pmatrix} \tag{3.17}$$

where P_i^2 for each point (x_i, y_i) is defined as:

$$P_i^2 = 2\sigma^2 \ln(I_i - N_B) \tag{3.18}$$

The standard deviation of the Gaussian distribution that is required for FluoroBancroft localization can either be measured by least-squared fitting of an appropriate reference sample or estimated with the help of the Rayleigh criterion using equation 3.19:

$$\sigma = \frac{0.61}{\sqrt{2}} * \frac{\lambda}{NA} \tag{3.19}$$

with the numeric aperture of microscope objective NA and the emission wavelength of the fluorescent source λ. Of course, the latter method is an approximation but usually delivers good results for σ. However, the selection of the right standard deviation value is quite important for FluoroBancroft localizations as too large errors of σ will inevitably result in localization errors and artefacts.

3.3.2.2 Realization

The programme for STORM/PALM data evaluation according to the FluoroBancroft algorithm was written in LabView 2009 (v 9.0, National Instruments) and is schematically visualized in fig. 3.11:

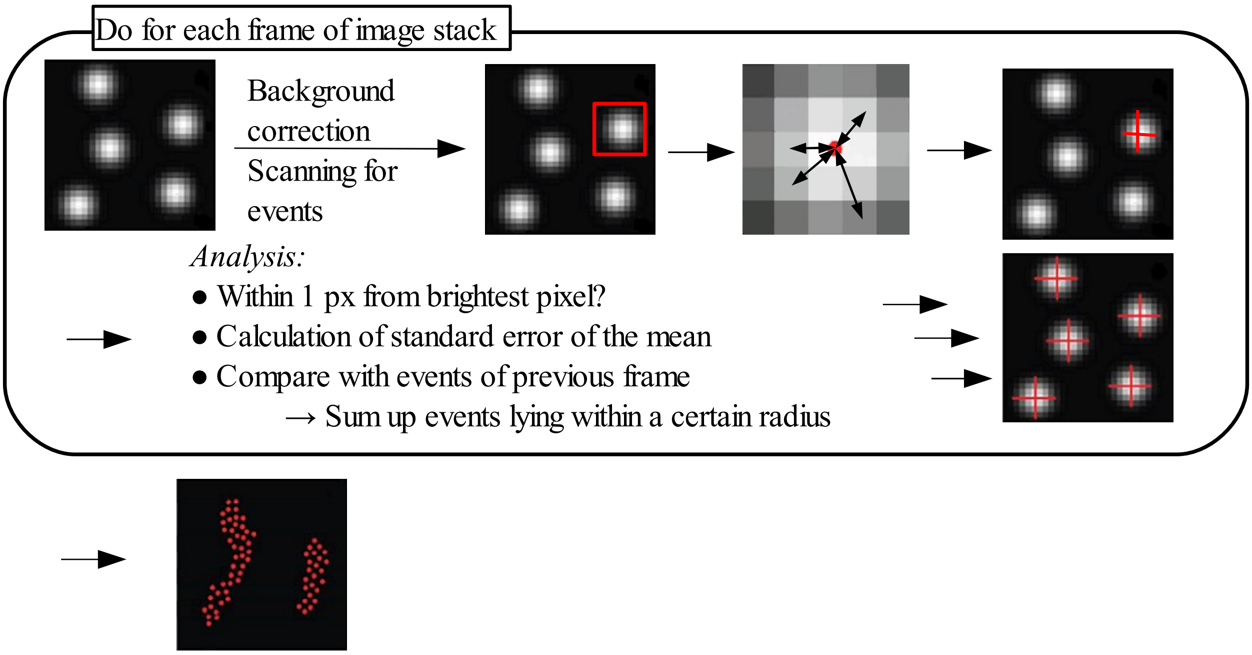
Do for each frame of image stack
Background correction
Scanning for events
Analysis:
● Within 1 px from brightest pixel?
● Calculation of standard error of the mean
● Compare with events of previous frame
→ Sum up events lying within a certain radius

FIGURE 3.11: SCHEME OF THE FLUOROBANCROFT PROGRAMME, PICTURES TAKEN FROM [38]

In the first step, each frame of the image stack from the measurement is corrected for camera offset and background noise. This corrected image is now scanned for events which exceed an intensity threshold defined by the user and whose size lies within a range between 5 and 20 pixels. If the event detection process has to be improved, e.g. due to high background noise, a filter can be applied to the image. Beside of the tools the FluoroBancroft programme offers (Median subtraction, Local background correction or Median Filter), other filters can be applied to the image stack by other programmes and then loaded into the analysis programme by choosing the 'Manual' option in the filter selection tool.

Every detected event is then checked if the signal-to-noise-ratio is below a certain value (typically < 3-fold). If so, the event is discarded. Otherwise, the original non-filtered image is localized by the described FluoroBancroft algorithm using four control points for the calculation. When choosing these points it is important to keep in mind that the respective distances to the brightest pixel are not larger than the standard deviation applied for this evaluation. If some or even all the control points lie outside the area covered by the Gaussian function, this will lead to large localization errors as the simulations in chapter 3.3.3.2 will demonstrate.

When the localization process has been performed, it is subsequently checked if the distance between the calculated centroid position and the brightest pixel of this localization event exceeds 1 px. In this case, the event will be discarded as this would mean that the localized centroid would lie outside of the brightest pixel. Additionally, the standard error of the mean according to equation 3.11 is calculated.

In the next step, the position of the detected event is compared to the events found in the previous frame. If there is also a localization within a certain distance range (usually 1 px), it is assumed that these events arise from the same molecule and are subsequently summed up. If events are found that are only appearing in one single frame, these localizations will be excluded from reconstruction as it is possible that these signals do not come from a sample dye molecule but are spontaneous and unspecific blinking or come from some free dye molecules diluted in the imaging buffer. In this way, all the other events detected in this frame are analysed, before proceeding to the next frame. When the whole stack has been analysed, the final image can be reconstructed analogue to the 2D Gaussian method.

3.3.3 Comparison of both localization methods

3.3.3.1 Calculation speed

In order to determine the difference in calculation speed between the FluoroBancroft algorithm and 2D Gaussian Fitting, a measured sample of 200 nm sized polystyrene beads was evaluated and the calculation time compared for different numbers of events (cf. fig.3.12).

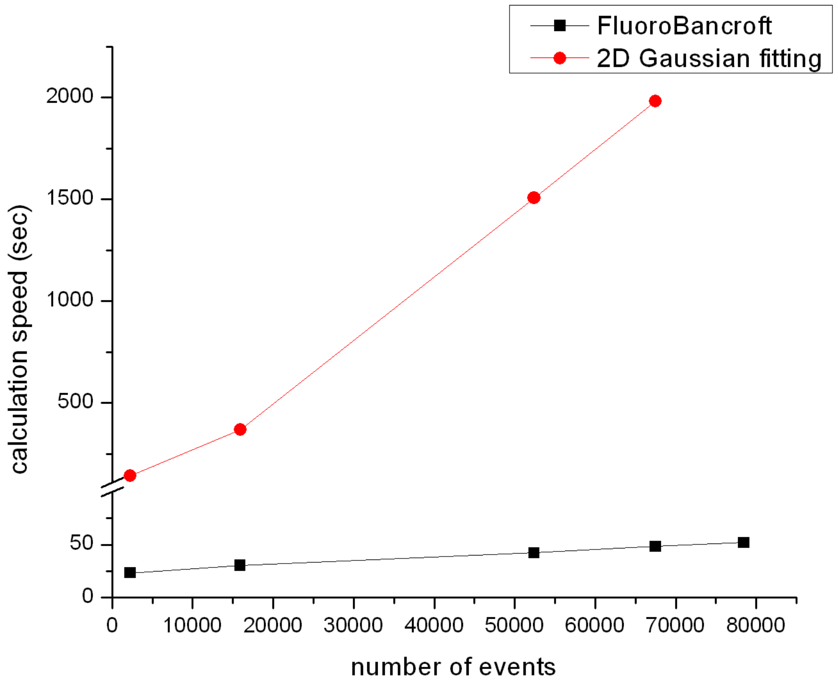

Figure 3.12: Speed improvement of localization by using FluoroBancroft algorithm

For the evaluations performed on the used computer systems (AMD Athlon 64x2 Dual Core Processor 6000+, 3.00 GHz), FluoroBancroft could achieve 2,700 localizations per second while there were only 35 localizations per second for the 2D Gaussian fitting procedure which means a speed improvement of a factor of 77 when using FluoroBancroft localization algorithm.

3.3.3.2 Data quality

Although the speed improvement demonstrated in the previous section means a significant advantage of the FluoroBancroft method compared to the 2D Gaussian fitting, it is also important to compare the localization quality of the two methods. For this reason, several tests were performed on simulated data. Therefore, an image with two-dimensional Gaussian signals was created according to the equation 3.20 where A = 500 and the intensity of each pixel follows a Poisson distribution.

$$I(x,y)=A+I_0 e^{\left[-\left(\frac{x-x_0}{\sigma_G}\right)^2-\left(\frac{y-y_0}{\sigma_G}\right)^2\right]/2} \tag{3.20}$$

By doing so, it was possible, on the one hand, to vary the width of the Gaussian over the standard deviation σ_G (assumed equal in x- and y-dimensions) and, on the other hand, to simulate different Siganl-to-Noise-ratios (SNR) by changing the amplitude of the Gaussian. The SNR was defined as

$$\mathrm{SNR} = I_0 \ / \ \mathrm{mean(Background)} \tag{3.21}$$

and the localization error was defined as the distance between the real position and the position found by the localization programme. For the standard deviation required for FluoroBancroft localization, σ_{FB}, the estimated value according to eq. 3.19 was used assuming an emission wavelength of 681 nm and a NA of 1.4 if not specified otherwise.

In the first experiment, the localization quality of the FluoroBancroft method and 2D Gaussian fitting procedure was compared using the different methods on the same data set, where the SNR was held constant (SNR = 5) and only the Gaussian standard deviation was varied. Fig. 3.13 shows the calculated localization errors for 2D Gaussian fitting and FluoroBancroft analysis. For the latter, in the first case, a fixed standard deviation σ_{FB} according to eq. 3.19 was used for localization. In the second case, several localizations with different values for σ_{FB} were performed for each σ_G. Subsequently, it was checked for which σ_{FB} the localization error was smallest for the respective σ_G (cf. table 3.3). The error of this localization was then used for plotting in fig. 3.13:

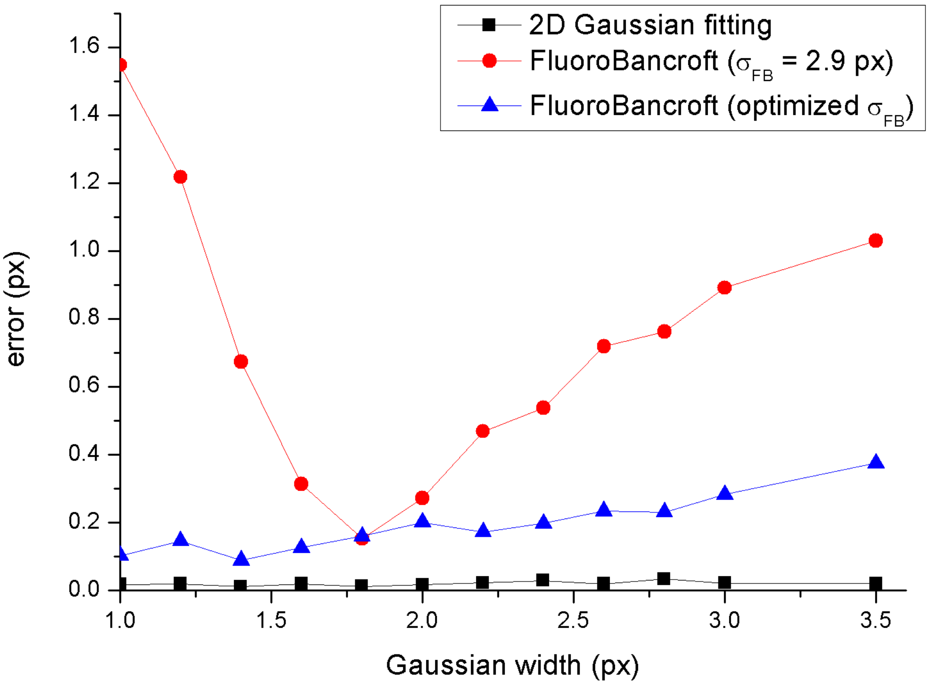

FIGURE 3.13: SIMULATED DATA, INFLUENCE OF GAUSSIAN WIDTH AT CONSTANT SNR (SNR = 5) ON LOCALIZATION ACCURACY FOR 2D GAUSSIAN FITTING, FLUOROBANCROFT ALGORITHM WITH FIXED RESP. OPTIMAL σ_{FB} FOR LOCALIZATION, EACH POINT REPRESENTING MEAN OF 10 LOCALIZATIONS

TABLE 3.3: OPTIMAL σ_{FB} FOR RESPECTIVE σ_G

σ_G	optimal σ_{FB}	σ_G	optimal σ_{FB}
1.0 px	2.0 px	2.2 px	3.5 px
1.2 px	2.2 px	2.4 px	3.8 px
1.4 px	2.4 px	2.6 px	4.0 px
1.6 px	2.6 px	2.8 px	4.2 px
1.8 px	2.9 px	3.0 px	4.6 px
2.0 px	3.0 px	3.5 px	5.2 px

The results of this experiment show that obviously 2D Gaussian fitting is not affected by the width of the simulated signal showing an error smaller than 0.1 px for all values. For the microscope setup used in this study (pixel size = 68 nm), this value corresponds to an error of 6.8 nm.

In contrast, a strong dependence is visible for the FluoroBancroft results when all localizations independent from the actual size σ_G are performed with the same value for σ_{FB}. Here, a high localization error can be observed for small Gaussians. When the Gaussian width increases, the error first gets lower before rising again after passing a minimum. This behaviour can be explained by looking at the shape of the different sized Gaussians as depicted in fig. 3.14:

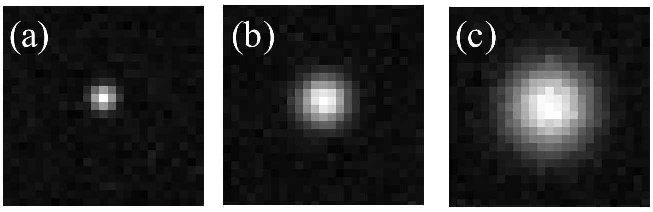

FIGURE 3.14: SIMULATED GAUSSIANS WITH DIFFERENT STANDARD DEVIATIONS: (a) $\sigma_G = 1$ PX, (b) $\sigma_G = 2.0$ PX, (c) $\sigma_G = 3.4$ PX

When there is a very small Gaussian, it is most likely that the control points, where the intensity values for FluoroBancroft localization are taken, lie outside of the area covered by the function so that the measured intensities do not give enough information about the Gaussian to localize the Gaussian exactly. For large σ_G, a similar argument can be applied: as the function is very broad, it also shows a relatively flat shape especially near the centroid. But as this is the area where the control points are usually situated, the information content is also low. This can be understood when considering that here a deviation in space does not result in a significant change of the measured intensity but of the distance from the centroid.

In contrast, the localization accuracy of FluoroBancroft algorithm can be improved significantly when the optimal parameter for σ_{FB} is used which lies in a range between $\sigma_G + 1$ px and

σ_G + 1.5 px depending on σ_G (cf. table 3.3). However, the error of the FluoroBancroft method still increases with the size of the Gaussian. For large σ_G, the 2D Gaussian fitting procedure still shows considerably better results (an error of 0.02 px compared to 0.37 px for FluoroBancroft algorithm at $\sigma_G = 5$ px). Nevertheless, the improvement compared to the FluoroBancroft evaluation with a fixed σ_{FB} is apparent.

In order to make sure that these results are not specific for the selected SNR value, another set of data was simulated where, contrary to the previous example, the Gaussian width was hold constant and the localization error was measured as a function of the SNR:

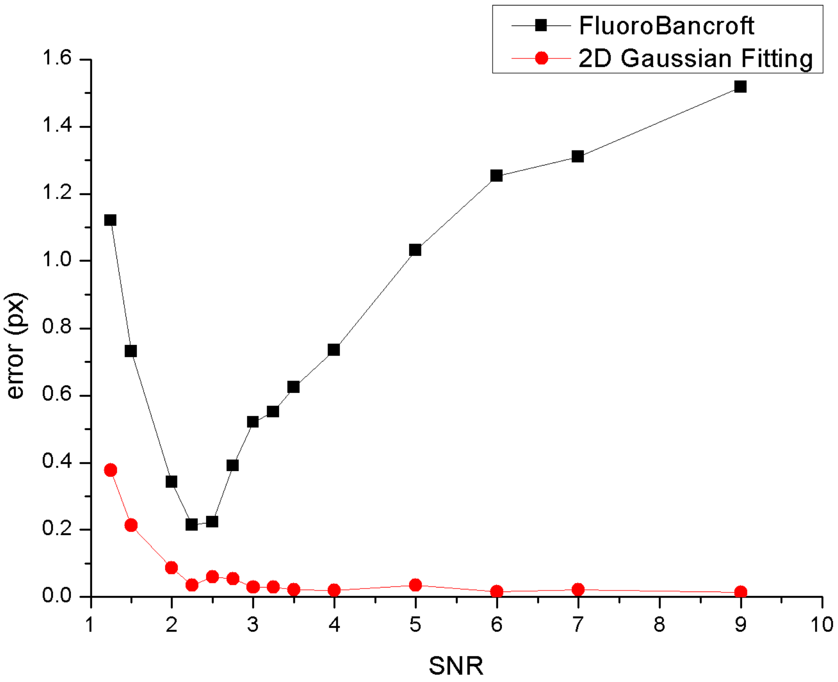

FIGURE 3.15: SIMULATED DATA, INFLUENCE OF SNR AT CONSTANT σ_G = 1.25 PX ON FLUOROBANCROFT AND 2D GAUSSIAN LOCALIZATION ACCURACY, EACH POINT REPRESENTING MEAN OF 10 LOCALIZATIONS

The results in fig. 3.15 clearly show that localization quality of the 2D Gaussian fitting method is not influenced much by SNR with exception of very low SNR where the localization error increases as the observed signal starts to merge with the background, but for higher SNR the localization error does not exceed 0.1 px (6.8 nm at a pixel size of 68 nm). This result therefore lies in the range of the resolution limit observed for PALM and STORM experiments of about 20 nm [8].

The course of the curve for FluoroBancroft localization seems to be a bit surprising as it should be intuitively expected that image quality should become better, when the SNR is increasing. However, this is only the case for very small SNR. Then, after passing a minimum at SNR = 2.5, the error increases again.

It is assumed that this observation can be explained by the fact that for high SNR and small Gaussians, as used here, the curve of the function shows a high steepness. Beside of the possibility that the measurement points might lie outside the function, it can be stated that a small change in space causes a significant change in the intensity measured at the control point which also leads to an considerable change in the calculated distance to the centroid.

In order to confirm this observation, further data sets for different SNR values and varying Gaussian widths were simulated and the respective events localized by FluoroBancroft algorithm. The results are shown in fig. 3.16:

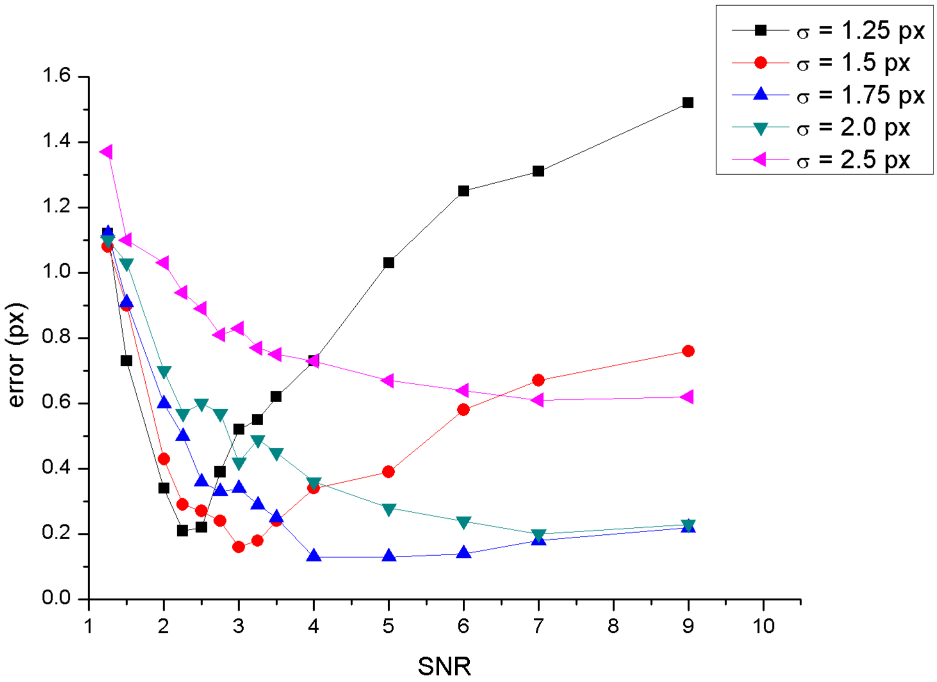

FIGURE 3.16: SIMULATED DATA, INFLUENCE OF GAUSSIAN WIDTH AND SNR ON FLUOROBANCROFT LOCALIZATION ACCURACY, EACH POINT REPRESENTING MEAN OF 10 LOCALIZATIONS

The diagram affirms the observations made in fig. 3.15: For small Gaussians, the localization accuracy seems to be better for low SNR, however, this behaviour changes when the Gaussian width exceeds a certain threshold of about 1.75 px: for these functions, the localization error decreases as expected when the SNR is increased. This observation supports the assumption that the large localization errors for small Gaussians at high SNR are due to the high steepness of the functions for high SNR as broad Gaussians do not show this phenomenon.

In order to test FluoroBancroft algorithm on real data, a further sample of HeLa microtubuli was recorded and the obtained data evaluated with the FluoroBancroft method where the results can be seen in fig. 3.17:

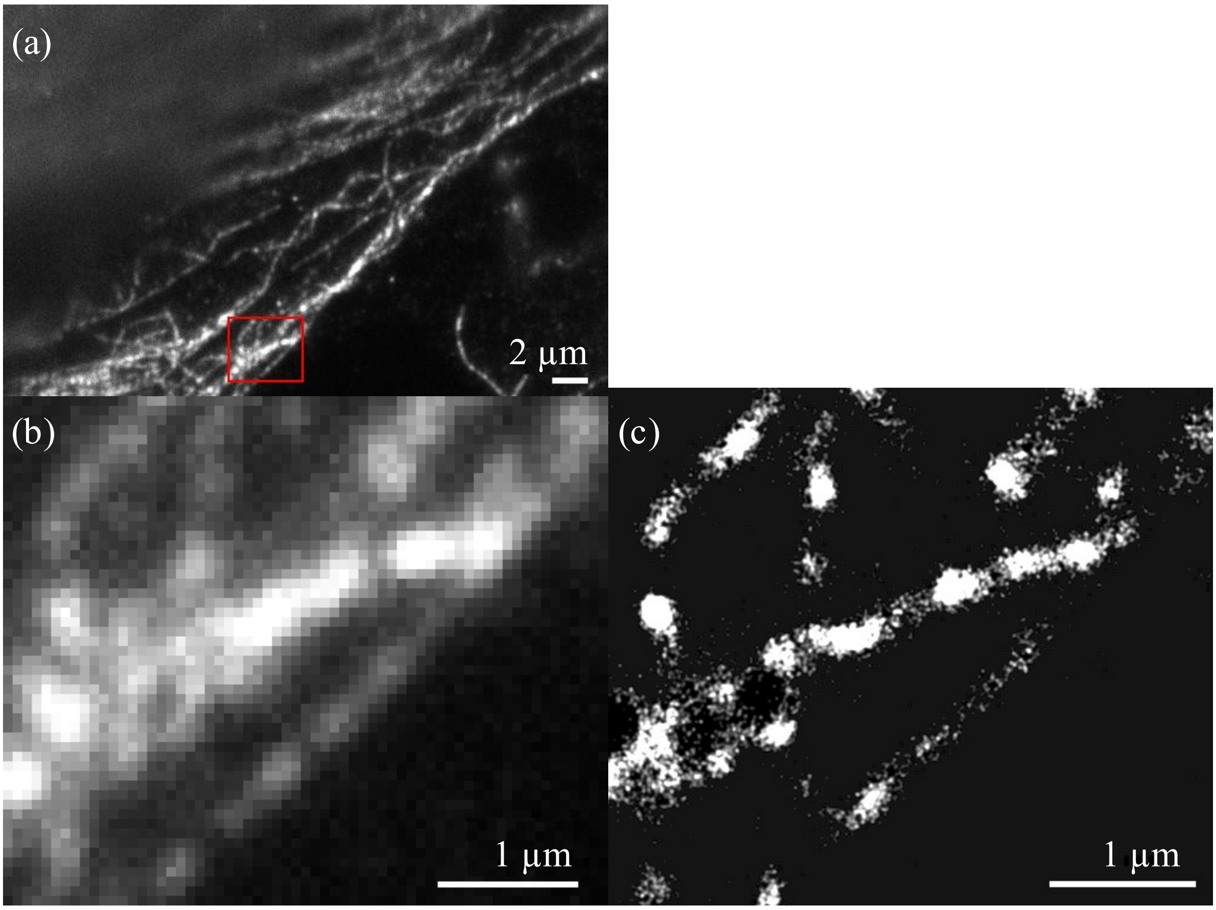

Figure 3.17: Demonstration of FluoroBancroft Reconstruction: HeLa cell labelled with β-tubulin antibodies labelled with Cy2 and Alexa Fluor 647: (a) Projection of reporting frames, (b) magnification of red crop in a), (c) FluoroBancroft reconstruction of b)

It can be stated that the reconstruction shown in fig. 3.17c gives a detailed image the structure of the microtubuli network, revealing more details than it is the case in the classical images, represented by the projection of the reporting frames in fig. 3.17b. The uneven point intensity that can be seen in the STORM image is not a consequence of the localization method but can be attributed to differences in the labelling densities of the used antibodies. The apparent fragmentation of the microtubuli might also be explained by cell fixation with paraformaldehyde (cf. methods section) as Robinson and Snyder showed in [40]. Therefore, using a different fixation reagent like e.g. methanol might also improve image quality.

Nevertheless, it could be shown that FluoroBancroft is a good high-speed alternative approach compared to the 2D Gaussian fitting method that delivers good results when it is kept in mind that its accuracy is much more dependent on the raw data quality than it is the case for the classical fitting.

3.3.4 Drift correction using cross correlation

In the last sections, it was shown that data evaluation with the presented methods delivered quite good results. However, there is one additional point that has be considered for the analysis of STORM or PALM data: As both methods exclusively depend on the localization of fixed emitters, it is very important that the fluorophores remain at the same place during a measurement, which means that there should be no sample drift. Numerous sources have to be taken into consideration for the origin of this drift, e.g. air currents, fluctuations in temperature or impurities on the sample holder, like traces of immersion oil. Especially the latter should be strictly avoided and the stage cleaned carefully after each measurement.

However, it is not always possible to prevent all these influences, as the following example demonstrates: Fig. 3.18 shows a crop from the measurement of a 40 nm polystyrene bead labelled with Cy2 and Alexa Fluor 647. While a) represents the image of the first frame taken, b) is the respective image from frame 17,000, which corresponds to a acquisition time of 15 minutes between these to frames at a frame rate of 55 ms. c) shows the merged images of both frames and points out the direction and scale of the occurring drift.

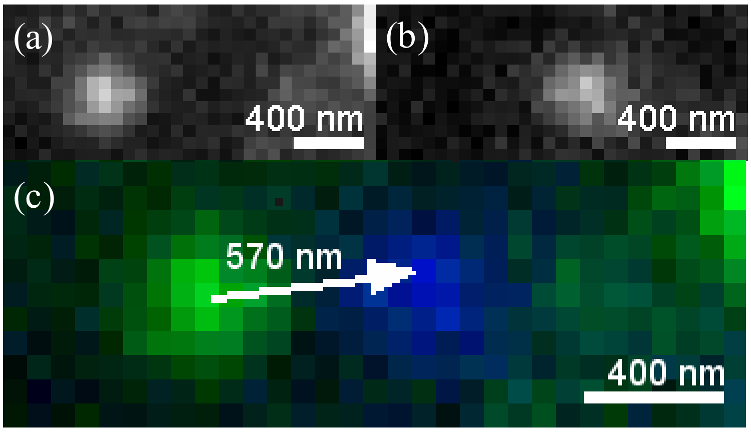

FIGURE 3.18: SAMPLE DRIFT: POSITION OF A 40 NM-BEAD IN FRAME 1 (a) AND FRAME 17,000 (b), (c) DIRECTION AND SCALE OF DRIFT BETWEEN a) AND b)

It is obvious that a correction of this data is necessary for high-resolution. In order to subtract out the effects of the drift of the reconstructed image, a correction programme was written by Volodymyr Kudryavtsev in LabView 2009 (v 9.0, National Instruments), where the magnitude of the drift was determined by performing an image cross correlation according to equation 3.22:

$$G_{mn}(x,y)=\frac{\sum_i\sum_j\left(I_m(i,j)I_n(i+x,j+y)\right)}{\left(\sum_i\sum_j\left(I_m(i,j)\right)^2\sum_i\sum_j\left(I_n(i+x,j+y)\right)^2\right)^{0.5}} \tag{3.22}$$

The normalized cross correlation function $G(x, y)$ compares the signals from two frames m and n

of the respective image stack. Each intensity from the first frame I_m at the position (i, j) is compared to the intensities I_n in the second frame at the position $(i+x, j+y)$. The expression in the numerator therefore will be large when $I_m(i, j)$ is similar to $I_n\ (i+x, j+y)$ for a certain variable pair x, y. The cross correlation will therefore reach its maximum when both images are identical. When there is no sample drift, this will be the case when $x = y = 0$. In contrast, when a linear drift occurs, the maximum will be found at other values for x and y. This fact can be used for drift correction when cross correlation is performed on two images of a stack and the maximum of the obtained cross correlation function is calculated by least-squared Gaussian fitting. The resulting values for x and y can subsequently be used for correction of the measured raw data.
In order to achieve good results, it is important to select a section of the respecting image stack where a signal can be found that does preferably not blink or bleach over the whole stack. For this purpose, non-bleaching markers like gold-beads can be fixed on the cover-slide additional to the sample. Otherwise, the programme is likely to start comparing signals to background noise which will evidently lead to errors as a lower similarity between the frames is assumed than existent.

Fig. 3.19 demonstrates the effect of drift correction on the quality of the reconstructed image. a) shows the non-corrected STORM image of the measurement depicted in fig. 3.18 and b) the same image after drift-correction.

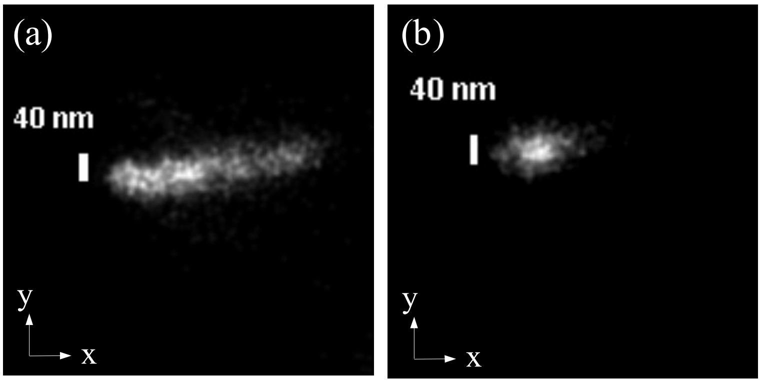

FIGURE 3.19: SAMPLE DRIFT: RECONSTRUCTED STORM-IMAGE (GAUSSIAN FIT) OF 40 NM-BEAD (a) BEFORE DRIFT-CORRECTION AND (b) AFTER DRIFT-CORRECTION

Comparing fig.3.19a) and b), it can be said that application of the presented cross correlation correction method results in a significant improvement of image quality as the spherical character of the bead now becomes visible. However, this example also shows that the potential of this technique is limited: while the size of the bead is reproduced well in y-direction (where no drift was observed during the measurement), the bead seems to be larger in x-direction which means that the drift could not be removed completely. In order to improve the correction, the additional fixation of a non-blinking reference as mentioned above might help.

This example demonstrates that it is always advisable to try to reduce all possible sources of drift before the measurement because a loss of image quality and image resolution cannot always be prevented entirely although the presented correction mechanism allows evaluation of images in which drift could not be avoided completely.

3.4 Discussion and outlook

STORM was established on the presented microscope system. The strong dependence of STORM on environment conditions was investigated and test experiments were performed to find the optimal conditions. Among other things, the best activation and deactivation rates for the reporter dyes is achieved when the pH of the imaging buffer is about pH = 8.

Data evaluation was successfully realized by 2D Gaussian Fitting as well as by the FluoroBancroft algorithm, which offers a fast alternative to numerical fitting. However, it could be demonstrated on simulated data that FluoroBancroft localization accuracy is much more sensitive to the quality of the data than Gaussian fitting. The results of FluoroBancroft are best when the intensities for the distance determination are taken at control points where the steepness of the respective Gaussian function is in a medium range. Also the localization error can be minimized by optimizing the standard deviation required for the calculation. In this case, the FluoroBancroft method is almost able to compete with the 2D Gaussian fitting procedure.

In summary, FluoroBancroft is an optimal method in order to get a quick insight in the quality of the sample and, for example, to select promising regions of a target, but these points should subsequently be fitted by Gaussians because of the generally lower errors of this method. Nevertheless, FluoroBancroft could be used for real time reconstruction that allows reconstructing the STORM image during the measurement process. Also other fast localization alternatives should be tested and compared to the FluoroBancroft algorithm and the 2D Gaussian fitting procedure, whose calculation speed should be tried to be increased further, e.g. by limiting the number of fitting parameters.

Several error correction tools were presented: For both localization methods, errors coming from photon noise, the finite size of the pixels and background noise could be corrected. For Gaussian fitting, also an ellipticity threshold was applied in order to discard bad events. Furthermore, it emerged as appropriate to discard events that are appearing in only one frame of the image stack as these signals are very likely caused by freely diffusing dyes or other non-desired signals. This tool was used for FluoroBancroft but should be implemented into the Gaussian fitting programme as well. Finally, a drift correction tool, implemented by Volodymyr Kudryavtsev, showed good results for improvement of image quality. In order to test STORM practically, high-resolution images of two test systems were obtained. 40 nm sized polystyrene beads and microtubuli of HeLa cells could be reproduced with very good results.

For the future, a new STORM setup will be built up, where emphasis will be placed on making the system as stable as possible. For example, the microscope stage is going to be completely self-constructed and critical parts will be made of Inwar, an iron-nickel alloy that shows almost no thermal expansion. Three-dimensional PALM and STORM imaging will be realized on this new system by including a cylindrical lens into the detection pathway of the microscope, as shown in figure 3.20:

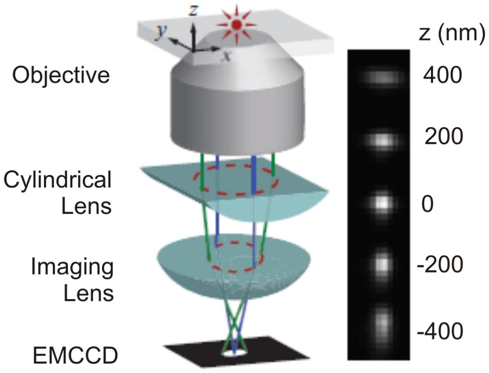

FIGURE 3.20: PRINCIPLE OF 3D-STORM: MOUNTING OF A CYLINDRICAL LENS INTO THE DETECTION PATHWAY (LEFT) INFLUENCES THE FORM OF THE PSF DEPENDING ON DEFOCUSSING (RIGHT), TAKEN FROM [29]

Implementation of the cylindrical lens creates two shifted focal planes for the x- and y-direction. The result is a change in the ellipticity and orientation of the PSF depending on the level of defocussing in z-direction. Thus, with the help of the observed shape of the PSF, the z-coordinate can be deduced. In previous experiments [29], the axial resolution could be increased with this method from 500-800 nm in classical optic microscopy up to 50-60 nm.

Another promising variant of STORM is an activator-reporter system with irreversible switching, therefore eliminating the main disadvantage of STORM compared to PALM. This could be realised by using covalent linked activator-reporter pairs. Here, each activator molecule is assigned to exactly one reporter. If this reporter is bleached, the activator is not able to activate any other molecules as it is the case in a standard STORM experiment where the dyes are distributed stochastically. In fact one of these pairs, consisting of Cy2 and Alexa Fluor 647, has already been synthesized [28] and is ready for testing.

4 Study of HIV budding by Super-Resolution Fluorescence Microscopy

In the last chapter, it was shown how PALM and STORM can be used to get high-resolution images of nanoscale structures. In order to demonstrate the relevance of these methods, we apply them to a system where their multi-colour approach can give information that would not be obtainable with other, non-optical high-resolution microscopy methods. For this purpose, the study of the budding process of HIV (Human immunodeficiency virus) was chosen.

4.1 Project overview and background

HIV is probably one of the most studied pathogens, however, there are still many questions open about the details of its life and reproduction cycle [41][42]. The virion budding is the step in the virus reproduction cycle that leads to the release of new virion particles from the infected cell. One important gene from the HIV genome [41] for this purpose is the so called group-specific antigen (*gag*). When this gene is expressed, it first exists in the form of a Gag-polyprotein, that consists of five subunits as shown in fig. 4.1. The cleavage of Gag into the single subunits does no take place until the virus matures, therefore the polyprotein is still uncleaved during the budding process.

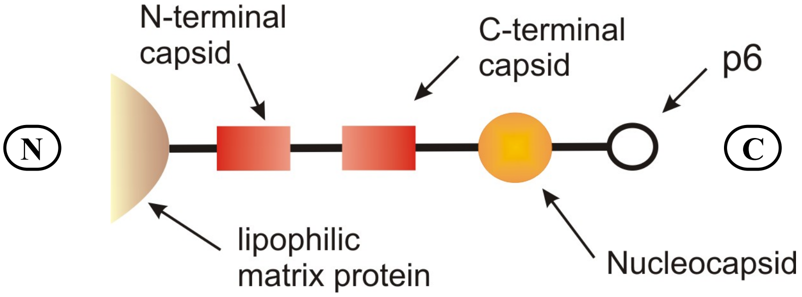

FIGURE 4.1: SCHEME OF THE INDIVIDUAL COMPONENTS OF THE GAG-POLYPROTEIN

In the first step of the budding process, the Gag-polyprotein reversibly binds to the cell membrane of the host cell with the help of its lipophilic matrix protein where the driving forces of this process are primarily ionic interactions between the lipids of the membrane and the protein. This binding is reversible but as there are also attractive interactions to other Gag-protein molecules caused by various intermolecular interactions, the cell membrane-protein complex is stabilized as soon as several Gag-proteins have attached to the membrane in close proximity. Finally, the aggregation of the Gag-proteins causes a bending of the cell membrane (as shown in fig. 4.2) which leads to the building of the virus bud.

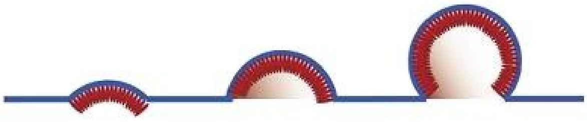

FIGURE 4.2: MEMBRANE BENDING INDUCED BY GAG-AGGREGATION, ADAPTED FROM [43]

For complete fission of the virus bud from the host cell, HIV requires parts of a cellular protein complex, the so called ESCRT-machinery (Endosomal Sorting Complexes Required for Transport) whose original task lies in the formation of Multi-Vesicular Bodies (MVB) but can be recruited by HIV. The ESCRT machinery consists of several components that are visualized in fig. 4.3. While the main tasks of ESCRT-0, ESCRT-I and ESCRT-II are the recognition and the sorting of the cargo that is going to be packed into the MVBs, ESCRT-III catalyses the fission of the particle from the membrane. The Vps4 complex finally is responsible for the disassembling of the ESCRT complex when the fission process is completed.

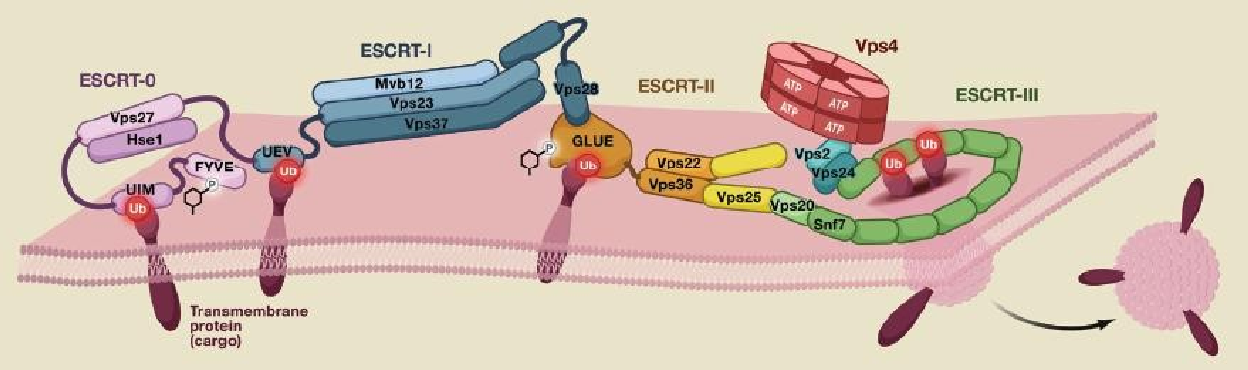
ESCRT-0
Vps27
Hse1
UIM
Ub
FYVE
P
UEV
Ub
ESCRT-I
Mvb12
Vps23
Vps37
Vps28
ESCRT-II
GLUE
P
Ub
Vps22
Vps36
Vps25
Vps20
Snf7
Vps4
ATP
ATP
ATP
ATP
Vps2
Vps24
Ub
Ub
ESCRT-III
Transmembrane protein (cargo)

FIGURE 4.3: SNAPSHOT OF THE YEAST ESCRT-MACHINERY, TAKEN FROM [44]

There are two pathways how Gag can recruit the human ESCRT machinery for budding. In both cases, the starting point is the p6-subunit of Gag: In the first case, the PTAP domain of p6 interacts with Tsg101 that is a part of ESCRT-I. Tsg101 (corresponds to Vps23 in yeast) is subsequently recognized by the Proline Rich Domain of ALIX (cf. fig. 4.4), another protein incorporated in the particle formation process, although it is not directly a part of ESCRT.

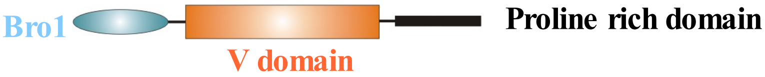
Bro1
Proline rich domain
V domain

FIGURE 4.4: DOMAINS OF ALIX PROTEIN

In the final step, ALIX domain Bro1 can recruit the CHMP4-subunits (Snf7 in yeast) of ESCRT-III (CHMP: Charged Multivesicular Body Proteins). Normally, this is the predominant mechanism, however, it is also possible that p6 recruits ALIX directly by interaction between the LYPX$_n$L-domain of Gag with the V-domain of ALIX also followed by Bro1 activating CHMP4.

The interactions of CHMP4 (existing in form of the isomers A, B and C) and Gag are now of particular interest for the understanding of the budding process mechanism as CHMP4 is one of the crucial components for particle fission from the cell membrane. If not activated, CHMP4 exists in monomeric form distributed in the cytoplasm. But as soon as it is recruited by ALIX, it starts to polymerize on the cell membrane at the budding site and to form ring-like structures that circle around the neck of the bud. Hanson *et al.* [45] could show these structures by electron microscopy: when they used a CHMP4B-GFP construct, they were able to observe rings built of CHMP4B with a hole in the middle as shown in fig. 4.5. These holes have a size of about 50 nm.

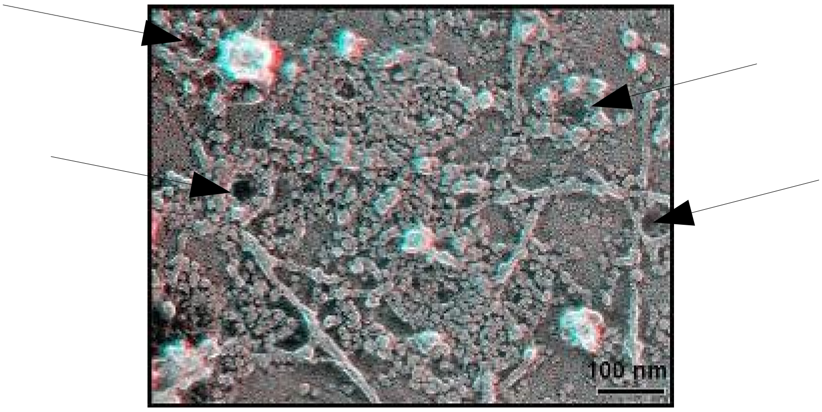

Figure 4.5: Electron microscope picture of CHMP4-GFP constructs, arrows point to CHMP4-ring structures, taken from [45]

However, they could not see these open form of the ring when using a CHMP4B-FLAG construct. It is known that tagging a fluorescent protein to CHMP4B leads to a dominant-negative form that effectively inhibits HIV particle release, which can be explained by the fact that large proteins like GFP block some of the functions of the ESCRT-III machinery [10].

The prior question remains is whether or not these structures can also be observed in wild-type systems as a part of the actual reproduction cycle of the virus. Furthermore, as EM can in general only deliver one-colour images, it is hardly possible to study the actual interactions between the CHMP4 proteins and the HIV-Gag protein.

4.2 Experimental approach

This system offers an ideal opportunity to show the resolution power of Super-Resolution-Fluorescence Microscopy because this method can resolve different structures with different colours. A multi-colour high-resolution approach was used to investigate the structure and interactions between CHMP4 and Gag.

In general, there are two different models discussed about how this interaction could be structured. The first one, presented by Lata, Weissenhorn *et al.* [46], suggests that the CHMP4-filaments are lying on the flat part of the cell membrane therefore building a ring around the neck of the budding site (cf. fig 4.6a) whereas the opposed model introduced by Wollert & Hurley [47] says that CHMP4 is situated at the inner part of the neck (cf. fig 4.6b).

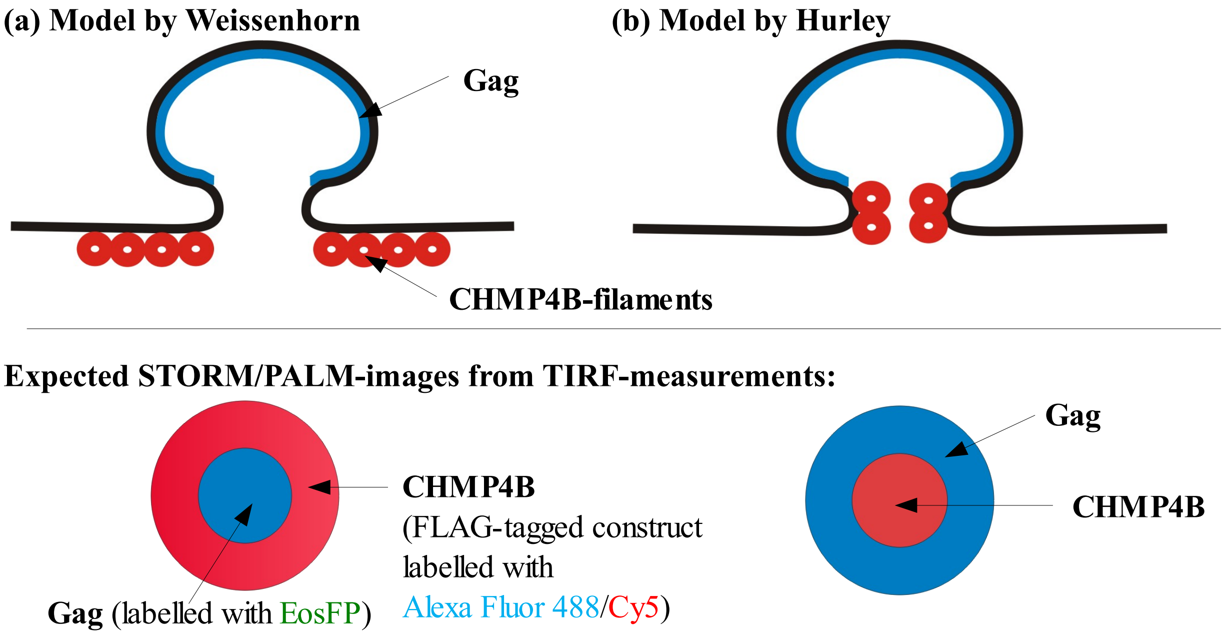
(a) Model by Weissenhorn

(b) Model by Hurley

Expected STORM/PALM-images from TIRF-measurements:

Figure 4.6: Different Models for Gag-CHMP4 interaction, design of STORM/PALM-experiments and expected high-resolution images for the respective models

In principal, it should be possible to decide between these two models by using two-colour high-resolution imaging as shown in the lower part of fig 4.6. In the first case, the Gag signal should be surrounded by a CHMP4B-ring, where, in the second case, the opposite is expected.

For this purpose, a combined STORM/PALM experiment was designed: Gag would be imaged by PALM by using a Gag-mEos construct. These construct contains the complete HIV genome with exception of the LTR control region in order to inhibit viral transcription. Additionally, it also encodes a variant of the photoswitchable EosFP. For the reconstruction of CHMP4B, it is not possible to do PALM because – as already mentioned – it is not possible to tag CHMP4B with fluorescent proteins without creating dominant-negative forms that are inhibiting HIV virion release. For this reason, it was necessary to do STORM. As there are no primary antibodies available against CHMP4B, a CHMP4B-FLAG construct provided by Goettlinger (University of Massachusetts Amherst) was used, were CHMP4B is fixed to a FLAG antigen.

Hence, CHMP4B could be labelled for STORM with the help of Anti-FLAG antibodies that were labelled with Alexa Fluor 488 and Cy5 as activator-reporter-pair.

4.3 Results

In the first experiment, the aim was to reconstruct the HIV particles as it was assumed that the PALM measurement should be gen erally easier to realize compared to STORM where numerous parameters have to be considered as the establishment of this method has already shown. HeLa cells were transfected with the Gag-mEos construct and observed under TIRF. The results of this experiment are depicted in fig. 4.7, where a) demonstrates the projection of the reporting frames at λ_{Exc} = 561 nm and b) is the reconstructed PALM image:

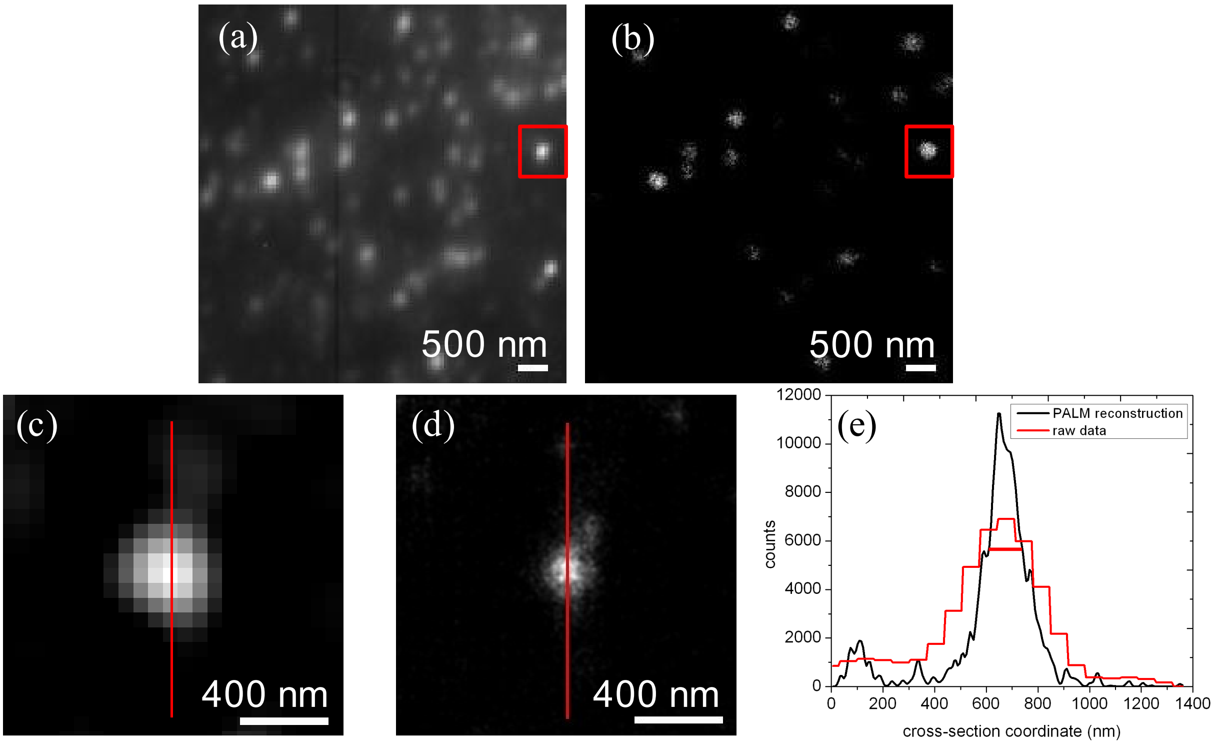
(a)
500 nm
(b)
500 nm
(c)
400 nm
(d)
400 nm
(e)
PALM reconstruction
raw data
counts
0
2000
4000
6000
8000
10000
12000
0
200
400
600
800
1000
1200
1400
cross-section coordinate (nm)

Figure 4.7: Gag-mEos reconstruction: (a) projection of reporting frames, (b) reconstructed PALM image (FluoroBancroft), (c) crop from a), (d) Gaussian reconstruction of crop from b) (e) cross-sectional profile for red lines in c) and d), red line shows a FWHM of PALM profile of 168 nm

Comparing a) and b), it can be seen that the reconstruction of Gag-mEos was successful. The spherical virus particles are clearly visible. From the cross-sectional profile shown in e), their size can be stated with about 170 nm which is in the range of values that can be expected [48].

However, when it was tried to cotransfect HeLa cells with Gag-mEos and the CHMP4B-FLAG construct in order to resolve the CHMP4-filaments and their interaction with Gag, it proved to be problematic to separate cells transfected with both constructs from those that were only transfected with one construct because both could be activated at $\lambda_{\text{Exc}} = 488$ nm (EosFP in its non-switched state and Alexa Fluor 488). For this reason, EosFP was exchanged for the next experiments by a Gag-mCherry construct. mCherry is a green fluorescing protein that has its absorption maximum at 586 nm and its emission maximum at 610 nm. In contrast to EosFP, mCherry is not photoactivable or photoswitchable, therefore it is not possible to obtain high-resolution PALM images of HIV from this system. However, this can be accepted as the main aim of the following experiment was the identification of colocalization spots of CHM4B and Gag-mCherry and a subsequent STORM image reconstruction of the respective CHMP4B sites.

In the following experiment, shown in fig. 4.8, HeLa cells were cotransfected with CHMP4B-FLAG and Gag-mCherry and studied under TIRF. The resulting projection of the reporting frames of the CHMP4B-STORM measurements was compared to the green signals from Gag-mCherry and scanned for colocalizations.

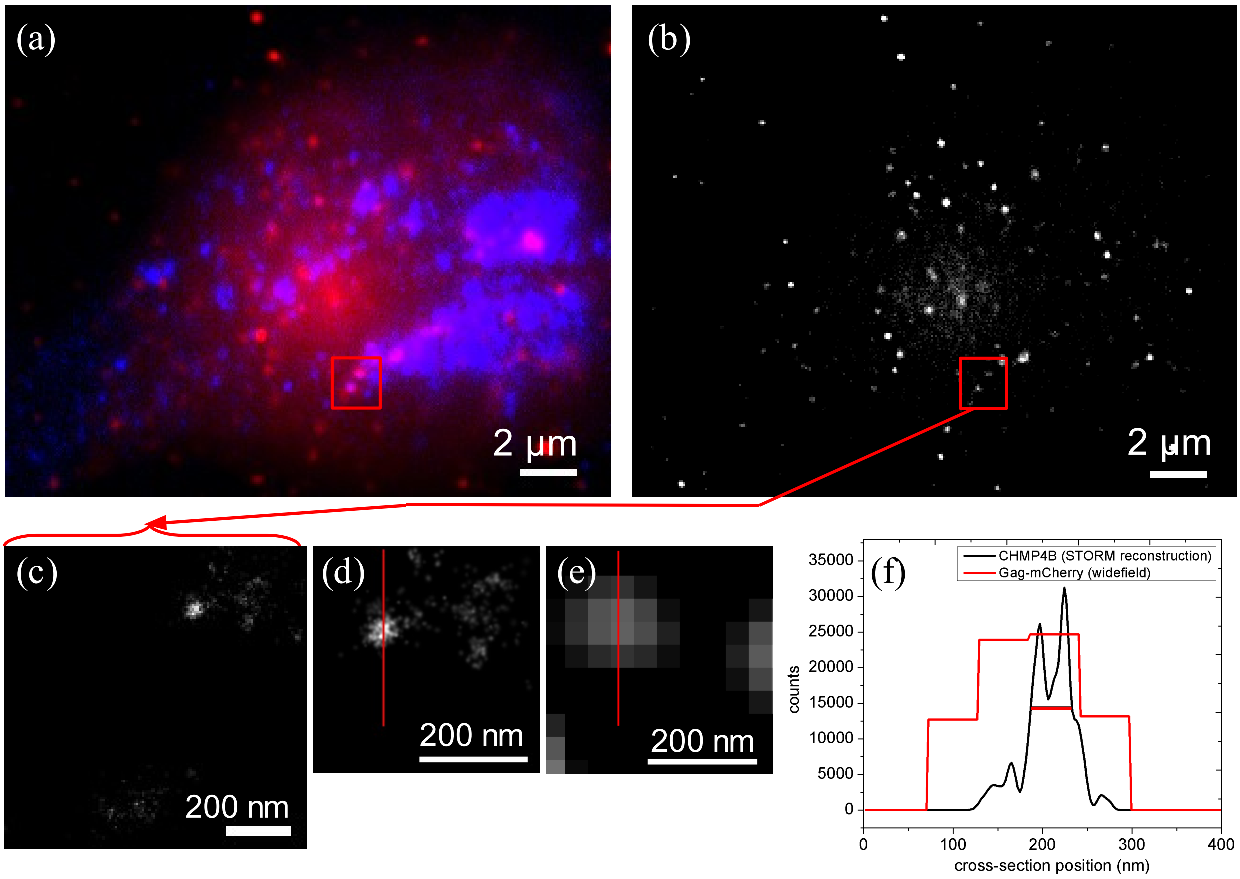

Figure 4.8: HeLa cell cotransfected with CHMP4B-FLAG and Gag-mCherry: (a) signal colocalization, (b) FluoroBancroft reconstruction, (c) 2D Gaussian reconstruction of red crop, (d) magnification of c), (e) respective section for Gag-mCherry, (f) cross-sectional profile along red lines in d) resp e), The red line shows a FWHM for CHMP4B of 55 nm

The composite of both images in a) shows signals in both channels, so it can be assumed that transfection was successful for both constructs. However, only a few colocalizations could be observed (e.g. particles in the red crop). A FluoroBancroft reconstruction was done for the complete image b) and promising spots (red crop) were selected. The Gaussian reconstruction from one of these spots, however, only revealed one object characterized by a size of 50 nm and a closed structure (c) and d)).

We should mention that the transfection efficiency seemed to be pretty low, so only about 5-10 cells showing signals for CHMP4B-FLAG could be found compared to an initial seeding density of $2*10^4$ cells per well. Nevertheless, it should be also taken into consideration that the low amount of signals might possibly depend on the performed staining with the labelled anti-FLAG antibodies. Therefore, several different types of these antibodies were tested where the following pictures show some examples of negative controls of non-transfected cells stained with the respective antibodies:

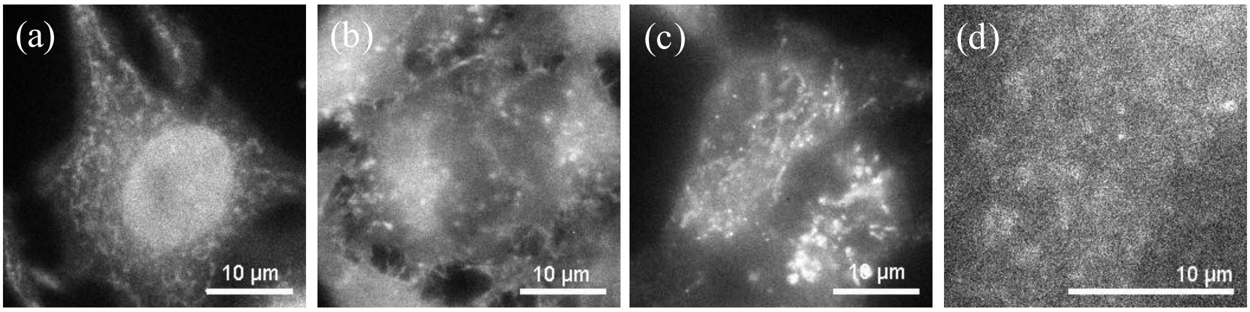

FIGURE 4.9: ANTIBODY TESTING: NEGATIVE CONTROLS LABELLED WITH (a) MOUSE MONOCLONAL, (b) RABBIT MONOCLONAL, (c) RAT MONOCLONAL AND (d) RABBIT POLYCLONAL ANTI-FLAG-ANTIBODIES

Especially in a), b) and c), a high amount of unspecific binding can be observed. The best results were actually achieved with the polyclonal antibody in d). For the monoclonal antibodies, the labelling concentration was drastically decreased, however, with exception of the rat antibodies there was no significant improvement.

Another problem, which had to be solved, was the low transfection efficiency for the CHMP4B-FLAG. In order to increase the number of transfected cells, various changes in the transfection protocol were applied. The final protocol, which is described in section 5.3.2, brought a reliable transfection rate but still at a very low level. In order to rule out errors in the DNA code, a sequencing of the CHMP4B-FLAG construct was performed. However, as the result did not give any evidence for such errors, a new purified sample of the construct will be used for future experiments.

In parallel, another strategy was pursued: Instead of labelling CHMP4B directly for the STORM experiment, the ALIX protein was used. As explained above, ALIX plays an important role at the recruitment of CHMP4B and *in vitro* experiments suggest that ALIX also seems to be responsible for stabilization of CHMP4B-filaments [49]. As CHMP4B also features a highly specific binding site for ALIX, it is assumed that ALIX tightly binds to activated CHMP4B. Furthermore, this system offers the advantage that primary antibodies for ALIX are available. Hence, no transfection is needed for imaging the CHMP4-structures and problems coming from overexpression caused by transfection are avoided and the system can be studied in its native state. HeLa cells were transfected with Gag-mCherry and subsequently stained with anti-ALIX antibodies labelled with Alexa Fluor 488 and Cy5. The result of one exemplary measurement can be seen in the fig. 4.10:

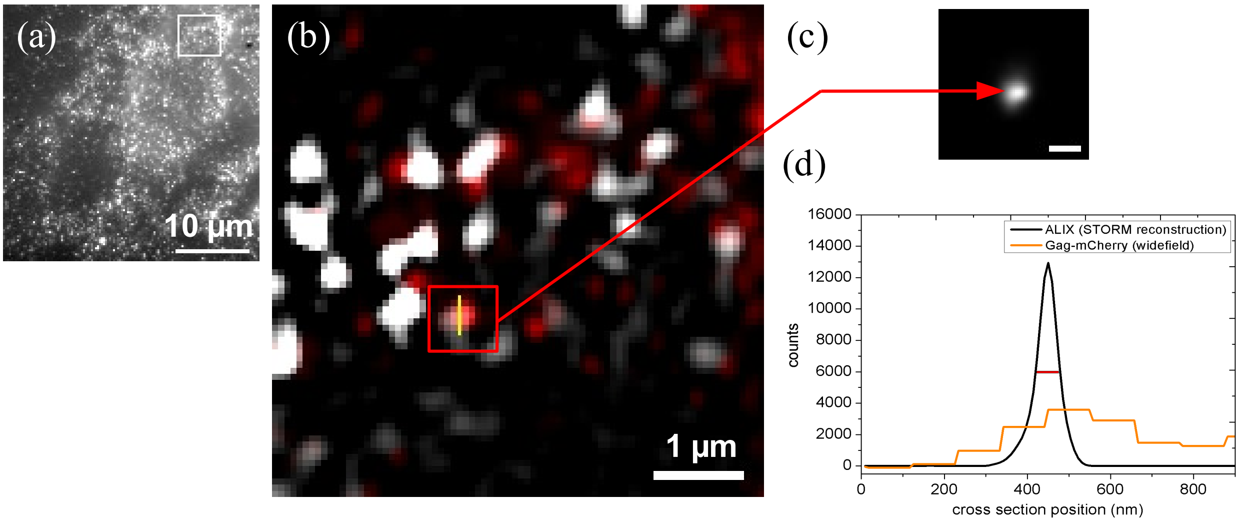

Figure 4.10: Gag-mCherry transfected HeLa cell, labelled with anti-ALIX antibodies (a) crop for localization study, (b) colocalization of Gag-mCherry (white) and ALIX (red), (c) 2D Gaussian reconstruction of red crop (scale: 100 nm), (d) cross-sectional profile of mCherry signal along yellow line in b) and of analogous spot in c) for ALIX, the red line shows a FWHM for ALIX of 58 nm

It was possible to observe some colocalizations of ALIX and Gag-mCherry as shown at the example of the evaluation of the white crop in a). But as the colocalization analysis in b) shows that the yield of usable events was not higher than for previous experiments with CHMP4B-FLAG. In c), reconstruction of such a localization event is demonstrated. d) shows the cross-sectional profiles for the signals in the red box shown in b). For Gag-mCherry the profile along the yellow line in b) was taken, for ALIX the corresponding line in c). The obtained object is similar in size and structure to the object observed in the CHMP4B-FLAG-experiment. It shows a closed, spherical shape and the size obtained from the FWHM of the ALIX cross-sectional profile is about 58 nm.

4.4 Discussion and outlook

The performed experiments showed that it is possible to reconstruct the HIV particles using PALM with a Gag-mEos construct, measuring a virus size of about 170 nm which matches well with the diameter of HIV known from literature [48]. For CHMP4B reconstruction, although transfection efficiency and labelling still have to be optimized, some transfected cells and colocalizations with Gag-mCherry on the cell surface could be imaged. On spots where STORM image reconstruction by 2D Gaussian fitting was possible, about 50-60 nm sized round, closed structures were found.

As an alternative to CHMP4B imaging, the ALIX protein, which is supposed to bind on CHMP4B, was labelled with appropriate antibodies. Again, colocalizations with Gag-mCherry were found in TIRF, but also with low yield. Nevertheless, the sites where STORM reconstruction could be done revealed similar, round and closed structures with approximately the same size as observed at the experiment with CHMP4B. It seems as if ALIX indeed binds to CHMP4B; however, due to the low colocalization yield, the question arises whether or not the binding occurs only in a certain stage of the budding process.

In summary, we see no evidence for the Weissenhorn model, as the images are more indicative for the Hurley model. However, this statement has to be treated with great care as much more budding sites have to be evaluated in order to get statistically significant results that can be used to verify a particular model. Therefore, an optimization, especially of the STORM measurements is necessary. The transfection efficiency of the CHMP4B-FLAG constructs needs to be increased and the antibody labelling improved. Furthermore, it would be promising to make two-colour measurements Gag-mEos and the labelled CHMP4B-constructs as it combines PALM and STORM, a combination which has not been shown in literature so far.

Two additional protein-protein interactions are of interest for further studies: The connection between CHMP4 and ALIX is of interest where many questions are still open concerning the role that ALIX actually plays in the stabilization of CHMP4. The experiments done in this field by Göttlinger *et al.* [49] were performed with a construct where an ALIX monomer was fused to a C-terminally deleted CHMP4B wild-type protein. EM images (cf. fig. 4.11) of this system showed that these modified CHMP4B-filaments dimerized when additional ALIX was added. However, it is unclear if the wild-type CHMP4B shows the same behaviour.

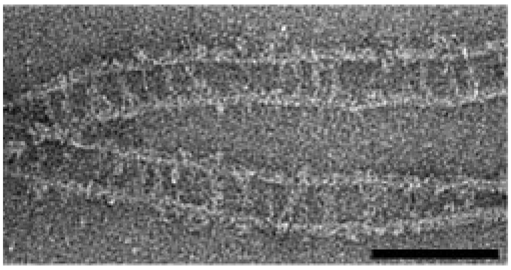

FIGURE 4.11: EM IMAGE OF CHMP4B-ALIX COMPLEXES (SCALE: 100 NM), TAKEN FROM [49]

Another interaction of interest is between CHMP4 and CHMP3 (Vps24 in yeast), a further subunit of ESCRT-III. According to the Weissenhorn model (cf. fig.4.12a), CHMP3 is believed to build capped filaments that support virus particle fission (cf. fig. 4.13), where in the Hurley model (cf. fig.4.12b) it only acts as a cap for the CHMP4-filaments. In the second case, only a few CHMP3 molecules would be necessary whereas the formation of the filaments in the Weissenhorn model would require much more of CHMP3.

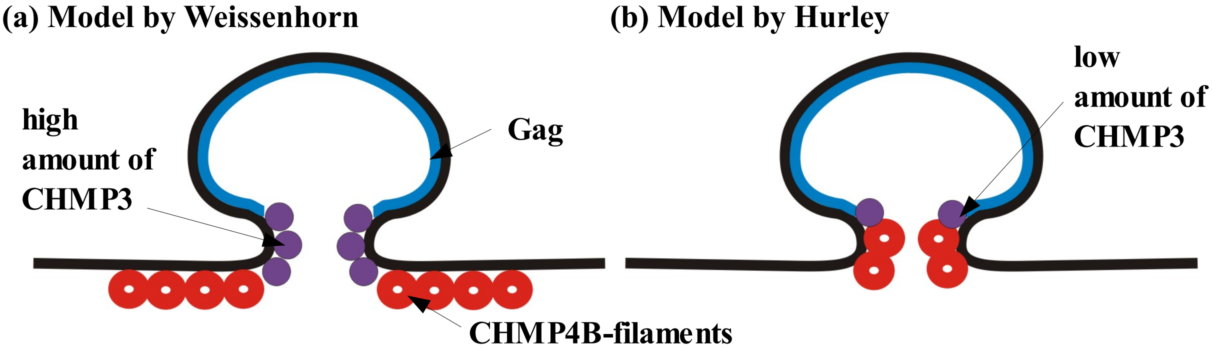

(a) Model by Weissenhorn
high amount of CHMP3
Gag
CHMP4B-filaments
(b) Model by Hurley
low amount of CHMP3

FIGURE 4.12: ROLE OF CHMP3 IN DIFFERENT BUDDING MODELS

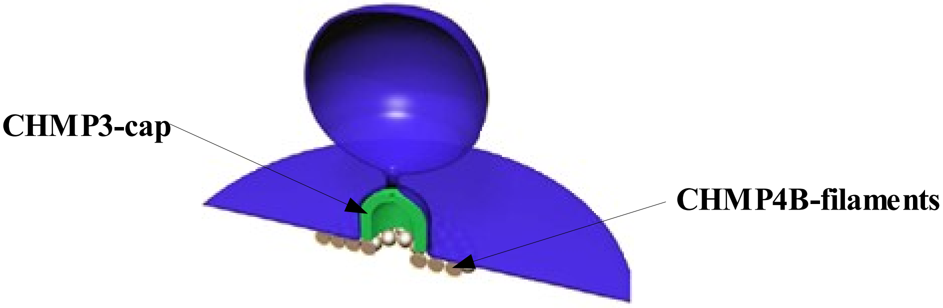

CHMP3-cap
CHMP4B-filaments

FIGURE 4.13: CHMP3-CAP (GREEN) IN WEISSENHORN'S MODEL, TAKEN FROM [50]

By labelling CHMP3-protein, it should be possible to differentiate between both models by the amount of CHMP3 that can be found in the STORM-images when doing a two-colour-STORM experiment with CHMP3 and CHMP4B.

5 Methods

5.1 Materials

The chemicals, enzymes, reagents and other materials used in this work are listed table 5.1:

Table 5.1: Overview over the materials and reagents used in this work

Substance	***Company***
anti-ALIX antibody (monoclonal (3A9))	antibodies-online GmbH
anti-FLAG antibody (monoclonal from mouse (M2))	Sigma-Aldrich
anti-FLAG antibody (monoclonal from mouse (Sig1-25))	Sigma-Aldrich
anti-FLAG antibody (polyclonal from rabbit)	Sigma-Aldrich
anti-FLAG antibody (monoclonal from rat)	Stratagene
anti-β-Tubulin antibody (monoclonal from mouse)	Invitrogen
Alexa Fluor® 647 carboxylic acid succinimidyl ester	Invitrogen
Alexa Fluor® 488 carboxylic acid succinimidyl ester	Invitrogen
BSA	Sigma-Aldrich
FluoSpheres biotin-labelled microspheres 0.2 µm (yellow-green-fluorescent (505/515))	Invitrogen
FluoSpheres neutravidin-labelled microspheres 0.04 µm (non-fluorescent)	Invitrogen
Catalase	Sigma-Aldrich
Cy2 bis-NHS-Ester	GE Healthcare
Cy5 bis-NHS-Ester	GE Healthcare
Dimethyl sulfoxide (anhydrous, 99.9%)	Sigma-Aldrich
FuGENE 6	Roche
D-Glucose	Sigma-Aldrich
Glucose oxidase	Sigma-Aldrich
Immersion oil 518F; $n_e = 1.518$ (23 °C), $u_e = 45$	Zeiss
2-Mercaptoethylamin	Fluka
β-Mercaptoethanol	Sigma-Aldrich
Opti-MEM (growing medium)	Invitrogen
Paraffin	Merck
Paraformaldehyde (16% w/v)	Electron Microscopy Sciences
Phosphate buffered saline (pH 7.5)	Invitrogen
Poly-L-Lysine	Sigma-Aldrich
Sodium bicarbonate	Fluka
Streptavidin	Invitrogen
Tris-HCl (pH 8.0)	Sigma-Aldrich
Triton X100	Fluka

Table 5.2 gives an overview over absorption and emission maxima and the extinction coefficients of the used organic dyes:

TABLE 5.2: SPECTRAL CHARACTERISTICS OF USED DYES

Dye	***Absorption maximum (nm)***	***Emission maximum (nm)***	***extinction coefficient ($cm^{-1}M^{-1}$)***
Cy2	489	506	150,000
Cy5	649	670	250,000
Alexa Fluor 488	495	519	71,000
Alexa Fluor 647	650	668	239,000

For cell transfection, a HIV-gag-mEos- and a HIV-gag-mCherry construct (provided by B. Müller and H.-G. Kräusslich from university medical centre Heidelberg, Department of Virology) were used. Both base on Gag wild-type 528 and encode the respective fluorescent protein and the complete HIV genome with exception of the LTR control region in order to inhibit viral transcription. Because of the removal of the latter, the *nef* gene is also non-functioning. The CHMP4B-FLAG-construct was provided by H. Goettlinger (University of Massachusetts Amherst). These constructs are coding the ESCRT-protein CHMP4B and a FLAG-antigene. Beside of this, the material listed in table 5.3 was used:

TABLE 5.3: OVERVIEW OVER ADDITIONAL USED MATERIAL

Material	***Company***
Performa DTR Gel Filtration Cartridges	EdgeBio
LabTek, LabTek II chamber slides	Thermo Fisher Scientific

UV/Vis-spectra were measured with a NanoDrop Spectrophotometer ND-1000 from peqLab Biotechnologie GmbH.

5.2 Buffers

An overview over the used buffers and their composition is given in tables 5.4 and 5.5:

TABLE 5.4: 150 mM $NaHCO_3$ BUFFER, 10x ENZYME STOCK, 50x GLUCOSE STOCK

	Component	*Concentration*	*Mass/Volume*
150 mM $NaHCO_3$-Buffer	$NaHCO_3$	150 mM	0.3780 g
	H_2O dd	-	30 mL
10x Enzyme Stock	Glucose oxidase (200 U/mg)	-	5 mg
	Tris-HCl (10x, pH 8.0)	-	100 µL
	H_2O dd	-	900 µL
	note: store at -78 °C		
50x Glucose Stock	Glucose	2.22 M	400 mg
	β-Mercaptoethylamine	2.50 M	193 mg
	H_2O dd	-	1000 µL
	note: store at -78 °C		

STORM Imaging Buffer

For the final imaging buffer, consisting of 8% (w/v) glucose, 50 mM β-mercaptoethylamine, 500 µg/mL glucose oxidase and 10 µg/mL catalase, the ingredients listed in table 5.7 are required:

TABLE 5.5: STORM IMAGING BUFFER

Component	*Volume*
10x Enzyme Stock	100 µL
Catalase (47000 U/mg)	0.8 µL
Tris-HCl (10x, pH 8.0)	100 µL
H_2O dd	780 µL
50x Glucose Stock	20 µL

It is important to note that the imaging buffer should always be prepared freshly before measurement. In particular, the glucose stock must not be added until the sealing of the chamber slides in order to maximize the effective period of the buffer.

5.3 Sample preparation

5.3.1 Preparation and fixation of streptavidin-labelled beads

a) Labelling of streptavidin with Cy2 and Alexa Fluor 647

At the beginning, 100 µL of a 149 µM streptavidin solution are equilibrated to a pH of about 8.2 by gel filtration chromatography using a *Performa DTR Gel Filtration Cartridge* equilibrated 4x with 150 mM $NaHCO_3$ buffer (centrifugation in each case with 750 x g for 2 min). In order to label the protein, 1.50 µL of a 50 mM solution of Cy2 bis-NHS ester (34.0 nmol; 30.5 µg) and 0.68 µL of a 50 mM solution of Alexa Fluor 647 carboxylic acid succinimidyl ester (75.0 nmol; ~93.8 µg) are added and the mixture is stored overnight at 4 °C. The labelled protein is then cleaned from remaining free dye molecules by another gel filtration chromatography using another *Performa DTR Gel Filtration Cartridge* equilibrated 4x with 150 mM $NaHCO_3$ buffer (centrifugation in each case with 750 x g for 2 min).

b) Labelling of 200 nm-beads with labelled streptavidin

20 µL of the bead stock (stock containing 1% solids, buffered at pH 7.5, coated with fluorescein-labelled biotin) are suspended in 835 µL Tris-HCl (pH = 7.5). The streptavidin, which was labelled in a), is mixed with non-labelled streptavidin in a ratio of 1 : 10. 45 µL of this solution are given to the prepared beads. After 10 minutes, in order to avoid unspecific bindings between the beads, 4 µL of a 10 mM biotin solution can be added optionally. The beads are spun down, the supernatant liquid is discarded and the beads are resuspended in Tris-HCl buffer.

c) Direct labelling of 40 nm-beads with Cy2 and Alexa Fluor 647

20 µL of the bead stock (stock containing 1% solids, buffered at pH 7.5, coated with neutravidin-labelled biotin) are suspended in 835 µL Tris-HCl (pH = 7.5). In the next step, 1.50 µL of a 50 mM solution of Cy2 bis-NHS ester (34.0 nmol; 30.5 µg) and 0.68 µL of a 50 mM solution of

Alexa Fluor 647 carboxylic acid succinimidyl ester (75.0 nmol; ~93.8 µg) are added.
The mixture is stored overnight at 4 °C before the beads are spun down at maximum speed (~ 5-10 minutes). The supernatant liquid is discarded and the beads are resuspended in Tris-HCl buffer.

d) Fixation of beads and preparation of the sample for measurement

At the beginning, 300 µL of Poly-L-Lysine are given to each well of a 'LabTek II'-chamber-slide and let adherent for 30 minutes. The wells are then washed two times with PBS buffer before the beads are added. After about 30 minutes, the liquid is removed and the beads are fixed for 15 minutes with 300 µL of a 4% v/v solution of paraformaldehyde in PBS. At the end, the wells are washed again two times with PBS, then filled with freshly prepared STORM imaging buffer and the chamber-slide is sealed airtight with paraffin.

5.3.2 Preparation and fixation of cell samples

a) Cell transfection

All cell experiments in this work were done with HeLa cells. In the first step, the transfection reagent FuGENE 6 is added to the Opti-MEM growing medium, with a transfection reagent concentration of 3% v/v. Furthermore, a 3:1 ratio between FuGENE 6 and DNA is used, meaning an amount of 3 µL FuGENE 6 would be required for 1 µg DNA. The mix is incubated for 5 minutes at room temperature. The respective amount of DNA is added and the resulting transfection complex is allowed to incubate for additional 20-30 minutes at room temperature. Finally, cell transfection is transformed by adding an appropriate amount of the transfection mix to the HeLa cell culture cultivated in a 'LabTek II'-chamber-slide well. Usually, at least 100 ng DNA per well are necessary (maximal 200 ng). After transfection, the cell culture is incubated for 18-24 hours at 37 °C and 5 % CO_2. Table 5.6 gives an overview over the compounds needed for the transfection of 4 LabTek chamber-slide wells:

Table 5.6: Cell transfection protocol

compound	***amount***	
total amount of DNA	400 ng	800 ng
Opti-MEM	35 µL	70 µL
FuGENE 6	1.2 µL	2.4 µL
CHMP4B-FLAG construct	200 ng	400 ng
gag-mEos *resp.* gag-mCherry construct	100 ng	200 ng
HIV wild-type 528	100 ng	200 ng

b) Labelling of anti-bodies

At the beginning, 100 µL (14.9 nmol, 100 µg) of the antibody diluted in PBS buffer are equilibrated to a pH of about 8.2 by gel filtration chromatography using a *Performa DTR Gel Filtration Cartridge* equilibrated 4x with 150 mM $NaHCO_3$ buffer (centrifugation in each case with 750 x g for 2 min). For labelling, the dyes listed in table 5.7 are used depending on the antibody which is going to labelled. In each case, the molar ratio of antibody : activator : reporter should be about 1 : 4 : 1.

Table 5.7: Overview over the activator- and reporter dyes used for the different antibody-labellings

Antibody	***Activator***		***Reporter***	
FLAG	Alexa Fluor 488 carboxylic acid succinimidyl ester	1.40 µL (5 mM)	Cy5 bis-NHS-ester	1.70 µL (5 mM)
β-Tubulin	Cy2-bis-N-hydroxysuccin-imidylester	3.33 µL (5 mM)	Alexa Fluor 647 carboxylic acid succinimidyl ester	0.83 µL (5 mM)
ALIX	Alexa Fluor 488 carboxylic acid succinimidyl ester	1.40 µL (5 mM)	Cy5 bis-NHS-ester	1.70 µL (5 mM)

The mixture is stored overnight at 4 °C and subsequently cleaned from unreacted dye molecules by performing another gel filtration chromatography using a *Performa DTR Gel Filtration Cartridge* equilibrated 4x with 150 mM $NaHCO_3$ buffer (centrifugation in each case with 750 x g for 2 min). At the end, the actual molar ratio of protein to dye, which is shown in table 5.8 is detected by a UV/Vis measurement.

TABLE 5.8: OBTAINED MOLAR RATIOS FOR HE DIFFERENT ANTIBODY-LABELLINGS

Antibody	***molar ratio protein : activator dye : reporter dye***
FLAG	1.00 : 2.97 : 1.56
β-Tubulin	1.00 : 1.93 : 1.27
ALIX	1.00 : 2.15 : 0.79

c) Protocol for antibody labelling and fixation of the cells

First, the growing medium is removed from the wells and the cells are fixed by adding 250 µL of a 4% v/v solution of paraformaldehyde in PBS to each well. After 15 minutes of fixation, the wells are washed two times with PBS before perforating the cell membrane by adding a 1 % v/v solution of Triton X100 detergent, diluted in PBS. After waiting 5 minutes, the wells are washed again two times with PBS.

In order to avoid unspecific binding of the antibodies, a BSA solution with a concentration of 2 mg/mL is given to each well and allowed to incubate for 30-60 minutes. Then, the BSA is removed and the cells are labelled by adding 150 µL of a solution of the labelled protein per well. The appropriate concentrations for the different antibodies are listed in table 5.9:

TABLE 5.9: AMOUNTS OF ANTIBODY REQUIRED FOR LABELLING

Antibody	***Concentration***
anti-FLAG (rabbit poly-clonal)	12 µg/1 mL
anti-FLAG (rat mono-clonal)	0.005 µg/1 mL
anti-β-tubulin	12 µg/1 mL
anti-ALIX	0.005 µg/1 mL

After 60 minutes of incubation, the wells are washed at least two times with BSA (2 mg/mL) where the sample is allowed to stand for 5 minutes after each washing step. Next, the wells are washed 2x with PBS and an additional fixation step is performed by giving 250 µL of a 4% v/v solution of paraformaldehyde in PBS to each well (incubate for 15 minutes). At the end, the wells are washed again two times with PBS, then filled with freshly prepared STORM imaging buffer and the chamber-slide is sealed airtight with paraffin.

6 Attachments

6.1 Abbreviations

BSA	Bovine serum albumin
CHMP	Charged Multivesicular Body Proteins
dd	double distilled
EMCCD	electron multiplying charge-coupled device
EM	electron microscopy
ESCRT	Endosomal Sorting Complexes Required for Transport
FWHM	full width at half maximum
Gag	Group-specific antigen
GFP	Green Fluorescent Protein
HIV	Human immunodeficiency virus
IC	Internal conversion
PSF	point spread function
TIRFM	Total Internal Reflection Fluorescence Microscopy
STORM	Stochastic Optical Reconstruction Microscopy
PALM	Photoactivated Localization Microscopy
PBS	phosphate buffered saline
PFA	paraformaldehyde

6.2 References

[1] Hooke, R. *Micrographia*; J. Martyn and J. Allestry: London, **1665**.

[2] Carpenter, W. B. *The microscope and its revelations*; J. & A.Churchill: London, **1901**.

[3] van Leewenhoeck, A. *Philosophical Transactions* **1677**, *12*, 821-831.

[4] Heimstädt, O. *Zeitschrift für wissenschaftliche Mikroskopie* **1911**, *28*, 330-337.

[5] Coons, A. H.; Creech, H. J.; Jones, R. N. *Proc. Soc. Expt. Biol. Med.* **1942**, *47*, 330-337.

[6] Ellinger, P.; Hirt, A. *Arch. Exp. Pathol. Phar.* **1929**, *147*(63), 63.

[7] Ploem, J. S. *Z. Wiss. Mikrosk.* **1967**, *68*, 129–142.

[8] Hell, S. W. *Nature Methods* **2009**, *6*(1), 24-32.

[9] Bates, M.; Huang, B.; Dempsey, G. T.; Zhuang, X. *Science* **2007**, *317*(5845), 1749-1753.

[10] von Schwedler, U. K.; Stuchell, M.; Müller,B.; Ward, D. M.; Chung, H.; Morita, E.; Wang, H. E.; Davis, T.; He, G.; Cimbora, D. M.; Scott, A.; Kräusslich, H.; Kaplan, J.; Morham, S. G.; Sundquist, W. I. *Cell* **2003**, *114*(6), 701-713.

[11] Lakowicz, J. R. *Principles of Fluorescence Spectroscopy*; Springer: New York, **2006**.

[12] Naredi-Rainer, N. *Multi Parameter Fluorescence Spectroscopy -Setup, Assembly and Applications*. Diploma thesis, Ludwig-Maximilians-Universität, München, **2009**.

[13] Sparrow, C. M. *The Astrophysical Journal* **1916**, *44*, 76-86.

[14] Gustafsson, M. *Current Opinion in Structural Biology* **1999**, *9*(5), 627-634.

[15] Ross, S. T.; Schwartz, S.; Fellers, T. J.; Davidson, M. W. *Nikon MicroscopyU.* http://www.microscopyu.com/articles/fluorescence/tirf/tirfintro.html (accessed 02/08/2010).

[16] Rust, M. J. ; Bates, M.; Zhuang, X. *Nature Methods* **2006**, *3*(10), 793-795.

[17] Betzig, E.; Patterson, G. H.; Sougrat, R.; Lindwasser, W.; Olenych, S.; Bonifacino, J. S.; Davidson, M. W.; Lippincott-Schwartz, J.; Hess, H. F. *Science* **2006**, *313*(5793), 1642-1645.

[18] Zhuang, X. *Nature Photonics* **2009**, *3*(7), 365-367.

[19] Bates, M. ; Blosser, T. R.; Zhuang, X. *Phys. Rev. Lett.* **2005**, *94*(10), 108101.

[20] Heilemann, M.; van de Linde, S; Schüttpelz, M.; Kasper, R.; Seefeldt, B.; Mukherjee, A.; Tinnefeld, P.; Sauer, M. *Angew. Chem.* **2008**, *120*(33), 6266-6271.

[21] Dempsey, G. T.; Bates, M.; Kowtoniuk, W. E.; Liu, D. R.; Tsien, R. Y.; Zhuang, X. *J. Am. Chem. Soc.* **2009**, *131*(), 18192–18193.

[22] Shimomura, O.; Johnson, F. H.; Saiga, Y. *Journal of Cellular and Comparative Physiology* **1962**, *59*(3), 223-239.

[23] Shaner, N. C.; Steinbach, P. A.; Tsien, R. Y. *Nature Methods* **2005**, *2*(12), 905-909.

[24] Wiedenmann, J.; Ivachenko, S.; Oswald, F.; Schmitt, F.; Röcker, C. ; Salih, A.; Spindler, K.; Nienhaus, G. U. *PNAS* **2004**, *101*(45), 15905–15910.

[25] Fellers, T. J.; Davidson, M. W. *Concepts in Digital Imaging Technology - Electron Multiplying Charge-Coupled Devices (EMCCDs)*. http://www.microscopy.fsu.edu/primer/digitalimaging/concepts/emccds.html (accessed 04/08/2010).

[26] Robbins, M. S. *IEEE Transactions on Electron Devices* **2003**, *50*(5), 1227-1232.

[27] Wickels, S.internship report, Ludwig-Maximilians-Universität, München, **2009**.

[28] Prescher, J.; Ivachenko, S.; Lamb, D. C. *unpublished results.*

[29] Huang, B.; Wang, W.; Bates, M.; Zhuang, X. *Science* **2008**, *319*(5903), 810-813.

[30] Mortensen, K. I.; Churchman, L. S.; Spudich, J. A.; Flyvbjerg, H. *Nature Methods* **2010**, *7*(5), 377-381.

[31] Thompson, R. E.; Larson, D. R.; Webb, W. W. *Biophysical Journal* **2002**, *82*(5), 2775–2783.

[32] Cronin, B.; de Wet, B.; Wallace, M. I. *Biophysical Journal* **2009**, *96*(7), 2912-2917.

[33] Löffler, G.; Petrides, P. E. *Biochemie und Pathobiochemie*; Springer: Berlin, **1998**.

[34] Rothbauer, U.; Zolghadr, K.; Tillib, S.; Nowak, D.; Schermelleh, L.; Gahl, A.; Backmann, N.; Conrath, K.; Muyldermans, S.; Cardoso, M.C.; Leonhardt, H. *Nature Methods* **2006**, *3*(11), 887-889.

[35] Wolter, S.; Schüttpelz, M.; Tscherepanow, M.; van de Linde, S.; Heilemann, M.; Sauer, M. *Journal of Microscopy* **2010**, *237*(1), 12-22.

[36] Smith, C. S.; Joseph, N.; Rieger, B.; Lidke, K. A. *Nature Methods* **2010**, *7*(5), 373-376.

[37] S. B. Andersson *Optics Express* **2008**, *16*(23), 18714-18724.

[38] Hedde, P. N.; Fuchs, J.; Oswald, F.; Wiedenmann, J.; Nienhaus, G. U. *Nature Methods* **2009**, *6*(10), 689-690.

[39] A. Muschielok, J. Andrecka, A. Jawhari, F. Brückner, P. Cramer, J. Michaelis *Nature Methods* **2008**, *5*(11), 965-971.

[40] Robinson, R. W.; Snyder, J. A. *Histochemistry and Cell Biology* **2004**, *122*(), 1-5.

[41] Greene, W. C.; Petetlin, B. M. *Nature Medicine* **2002**, *8*(7), 673-680.

[42] Samuel, C. E. *The Journal of Biological Chemistry* **2006**, *281*(13), 8305-8307.

[43] Carlson, L.; Briggs, J. A. G.; Glass, B.; Riches, J. D.; Simon, M. N.; Johnson, M. C.; Müller, B.; Grünewald, K.; Kräusslich, H. *Cell Host & Microbe* **2008**, *4*(6), 592-599.

[44] Teis, D.; Saksena, S.; Emr, S. D. *Cell* **2009**, *139*(1), 812.

[45] Hanson, P. I.; Roth, R.; Lin, Y.; Heuser, J. E. *The Journal of Cell Biology* **2008**, *180*(2), 389-402.

[46] Lata, S.; Schoehn, G.; Solomons, J.; Pires, R.; Göttlinger, H. G.; Weissenhorn, W. *Biochemical Society Transactions* **2009**, *37*, 156-160.

[47] Wollert, T.; Hurley, J. H. *Nature* **2010**, *464*(7290), 864-870.

[48] Fuller, S. D.; Wilk, T.; Gowen, B. E.; Kräusslich, H.; Vogt, V. M. *Current Biology,* **1997**, *7*(10), 729-738.

[49] Pires, R.; Hartlieb, B.; Signor, L.; Schoehn, G.; Lata, S.; Roessle, M.; Moriscot, C.; Popov, S.; Hinz, A.; Jamin, M.; Boyer, V.; Sadoul, R.; Forest, E.; Svergun, D. I.; Göttlinger, H. G.; Weissenhorn, W. *Structure* **2009**, *17*(6), 843-856.

[50] Fabrikant, G.; Lata, S.; Riches, J. D.; Briggs, J. A. G.; Weissenhorn, W.; Kozlov, M. M. *PLoS Computational Biology* **2009**, *5*(11), 1-11.